

Constraining the Envelope Structure of L1527 IRS: Infrared Scattered Light Modeling

John J. Tobin¹, Lee Hartmann¹, Nuria Calvet¹ & Paola D'Alessio²

ABSTRACT

We model *Spitzer Space Telescope* observations of the Taurus Class 0 protostar L1527 IRS (IRAS 04368+2557) to provide constraints on its protostellar envelope structure. The nearly edge-on inclination of L1527 IRS, coupled with the highly spatially-resolved near to mid-infrared images of this object and the detailed IRS spectrum, enable us to constrain the outflow cavity geometry quite well, reducing uncertainties in the other derived parameters. The mid-infrared scattered light image shows a bright central source within a dark lane; the aspect ratio of this dark lane is such that it appears highly unlikely to be a disk shadow. In modeling this dark lane, we conclude that L1527 IRS is probably not described by a standard TSC envelope with simple bipolar cavities. We find it necessary to model the dark lane and central source as a modified inner envelope structure. This structure may be due either to a complex wind-envelope interaction or induced by the central binary. To fit the overall SED, we require the central source to have a large near to mid-infrared excess, suggesting substantial disk accretion. Our model reproduces the overall morphology and surface brightness distribution of L1527 IRS fairly well, given the limitations of using axisymmetric models to fit the non-axisymmetric real object, and the derived envelope infall rates are in reasonable agreement with some other investigations. IRAC observations of L1527 IRS taken 12 months apart show variability in total flux and variability in the opposing bipolar cavities, suggesting asymmetric variations in accretion. We also provide model images at high resolution for comparison to future observations with current ground-based instrumentation and future space-based telescopes.

Subject headings: ISM: individual (L1527) — ISM: jets and outflows — stars: circumstellar matter — stars: formation

¹Department of Astronomy, University of Michigan, Ann Arbor, MI 48109; jjtobin@umich.edu

²Centro de Radioastronomía y Astrofísica, UNAM, Apartado Postal 3-72 (Xangari), 58089 Morelia, Michoacán, México

1. Introduction

The *Spitzer Space Telescope* has given us unprecedented views of star forming regions. With *Spitzer*, we are able to study the earliest stages of star formation with far greater resolution, sensitivity, and through higher extinctions than was previously possible with ground-based near-infrared (NIR) imaging. These capabilities of *Spitzer* enable us to test theories of star formation (e.g. Terebey et al. 1984; Shu et al. 1987) in detail using radiative transfer models (e.g. Whitney et al. 2003a). The Terebey et al. (1984, TSC) model, describes the collapse of an initially spherical envelope which becomes rotationally flattened as it collapses. This model has been the standard, most widely used, model describing infalling protostellar envelopes for the past two decades (e.g. Adams et al. 1987; Kenyon et al. 1993; Osorio et al. 2003; Whitney et al. 2003a; Robitaille et al. 2006; Furlan et al. 2007; Tobin et al. 2007).

Protostars drive powerful, bipolar molecular outflows which carve out cavities in the circumstellar envelope. These cavities can be observed as scattered light nebulae. The TSC envelopes alone predicted too little flux short ward of $10\mu\text{m}$, necessitating the inclusion of bipolar outflow cavities into the standard model (Calvet et al. 1994). Thus far, a simple bipolar cavity structure carved out of a TSC envelope has sufficed for modeling images and spectral energy distributions (SEDs) of evolved, Class I, protostars. However, recent observations by *Spitzer* are enabling us to perform detailed studies of outflow cavities and envelopes of the youngest protostars, the Class 0 objects (Andre et al. 1993). In particular, *Spitzer* observations of outflow cavities in scattered light permit more detailed analysis of the inner structure of protostellar envelopes.

Observations of protostars with the Infrared Array Camera (IRAC) (Fazio et al. 2004) have revealed numerous, prominent scattered light nebulae associated with Class 0 objects (e.g. Noriega-Crespo et al. 2004; Tobin et al. 2007; Seale & Looney 2008). Scattered light nebulae are also observed in J, H, and Ks (JHK) bands. However, the scattered light in JHK bands is highly attenuated by the dense circumstellar envelope, therefore scattered light nebula are often observed to appear brightest in the IRAC channels numbered 1 to 4 (3.6 , 4.5 , 5.8 , and $8.0\mu\text{m}$) (Tobin et al. 2007).

Scattered light images are an important, alternative method of probing the envelope structure of protostars, complementary to submillimeter and millimeter studies of optically-thin dust emission. IRAC images are important to scattered light studies because we can more clearly observe the envelope structure since the dust is less optically thick than at JHK bands. Scattered light images enable clear observation of the outflow cavities and may directly show the effects of the outflow on the envelope. In addition, submillimeter images tend to be elongated along the outflow cavities due to heating from the central protostar and disk. This additional emission complicates analysis of the envelope structure at long

wavelengths without knowledge of the outflow cavity structure from scattered light images.

We cannot derive most physical parameters from scattered light images alone. Radiative transfer modeling, in conjunction with a detailed observational analysis, must be performed to derive the likely physical parameters of an object. The results from radiative transfer modeling can yield insights into the structure of protostars that scattered light images or dust continuum observations alone would not reveal. Observations of L1527 IRS (IRAS 04368+2557) with the *Spitzer Space Telescope* are an ideal starting point for testing models of low-mass star formation.

The L1527 dark cloud is located within the Taurus molecular cloud at a distance of ~ 140 pc. This object has been observed extensively from the NIR to centimeter wavelengths (Ohashi et al. 1997; Chandler & Richer 2000; Loinard et al. 2002; Hartmann et al. 2005). L1527 IRS, hereafter L1527, is classified as a borderline Class 0/I object with a large, dense circumstellar envelope (Chen et al. 1995; Motte & André 2001), we will refer to L1527 as a Class 0 object. A unique property of L1527 is that it is observed at a nearly edge-on ($\sim 90^\circ$) inclination (Ohashi et al. 1997). The tightly constrained inclination makes L1527 ideal for modeling since the inclination-dependent degeneracies on other modeled parameters (e.g. luminosity, opening angle, infall rate) (Whitney et al. 2003b) are limited. Also, since L1527 is relatively nearby, the spatial resolution of the observations is about 2 times better than observations of protostars in Perseus and 3 times better than Orion.

The envelope properties of L1527 have been modeled previously. Kenyon et al. (1993) (KCH93) used TSC envelopes to model the SED from IRAS; Furlan et al. (2007) (F07) used a similar, improved model to fit the SED and MIR spectrum of L1527. Finally, Robitaille et al. (2007) (R07) modeled L1527 using a large grid of TSC models calculated by the Whitney et al. (2003a) code (Robitaille et al. 2006). Here we revisit L1527, performing a more comprehensive observational analysis using scattered light images, MIR spectra and photometry from the NIR to millimeter wavelengths. We use these data combined to construct a new, detailed model describing the envelope structure of L1527 in order to test star formation theories and gain a more clear picture of protostellar structure.

2. Observations and data reduction

2.1. Spitzer Space Telescope Data

Our data are taken from previous observations of Taurus in the *Spitzer* archive, processed with pipeline version S14.0.0. L1527 has been observed twice; first on 07 March 2004 as part of the guaranteed time observer (GTO) survey of known young stars in Taurus

(Hartmann et al. 2005) and again on 23 February 2005 as part of the Taurus Legacy survey (Padgett et al. 2006). The GTO observations were performed in a 3 position, cycled dither pattern, with a frame time of 12 seconds. The Legacy data mapped the entire Taurus region twice with single frames of 12 seconds each and spatial limited overlap. The legacy data of L1527 are comprised of two frames taken a few hours apart, which require manual processing. We re-mosaicked the data using MOPEX version 061507 to make combined images from both observations and to create a more clean mosaic of the Taurus Legacy data.

The Taurus legacy survey also observed L1527 with the Multiband Imaging Photometer (MIPS) (Rieke et al. 2004). The observations were carried out in mapping mode on 05 March 2005 in two separate observations of all three bands: 24, 70, and $160\mu\text{m}$. We used the post-BCD data for the $24\mu\text{m}$ observations; it was necessary to re-mosaic the $70\mu\text{m}$ data using filtered BCD images because the post-BCD data have gaps due to only half of the detector functioning. The $160\mu\text{m}$ data did not fully map L1527 and we could not use the data for photometry.

L1527 has also been observed by the Infrared Spectrometer (IRS) (Houck et al. 2004) onboard the *Spitzer Space Telescope*. The spectrum was taken in both orders of the short-low (5 - $14\mu\text{m}$) and long-low ($14 - 40\mu\text{m}$) modules on 27 February 2004. In our analysis, we use the same spectrum as presented in F07. The spectral resolution is $R \sim 120\text{-}60$ for both modules.

2.2. Near-Infrared Observations

We observed L1527 at the MDM Observatory at Kitt Peak on 27 and 29 December 2007 using the 2.4m Hiltner telescope with the NIR imager TIFKAM (Pogge et al. 1998). We observed L1527 in the J, H, Ks, and H_2 ($2.12\mu\text{m}$) filters on 27 December and the H_2 continuum ($2.09\mu\text{m}$) filter on 29 December; with total integration times in J and H-band of 10 minutes and a total integration time of 35 minutes in Ks, H_2 , and H_2 continuum bands. The H_2 continuum filter is a line-free, narrowband filter with a bandwidth matching the H_2 filter.

The observations were conducted in a 5 point dither pattern with 1 minute of integration per dither position. After each complete dither pattern, we chopped off source and observed the sky in the same 5 point dither pattern to construct a median sky. The off-source imaging was necessary because TIFKAM has a $3'$ field of view and L1527 nearly fills the field. The data were reduced using standard routines from the upsquid package for flat fielding, sky subtraction, and combining. Our J-band image does not detect L1527 and the H-band

image only marginally detects L1527. However, L1527 is clearly observed in the Ks-band image. The H₂ image marginally detects L1527 with comparable signal-to-noise (S/N) to H-band, while the H₂ continuum band image does not detect L1527.

2.3. Additional Infrared Data

We also included mid-infrared data from the Infrared Space Observatory (ISO) in our study. We used ISOCAM data from the 6.7, 9.6, 11.3 and 14.3 μm bands observed on 02 October 1997. These bands are overlapped by the IRS instrument, however, we used these images to constrain any extended emission at these wavelengths. We used pipeline processed data from the ISO science archive, performing no further reduction of these data.

Finally, we used data from the Two Micron All Sky Survey (2MASS) (Skrutskie et al. 2006) in our study of L1527. We use the calibrated data frames for the L1527 region from the 2MASS archive.

2.4. Photometry

We performed aperture photometry on L1527 using the Image Reduction and Analysis Facility (IRAF)¹. Photometry was not straightforward since a background annulus cannot be used because it includes extended emission surrounding the source. Instead, using the ‘imstat’ procedure in IRAF, we measured a large area of sky adjacent the source that was devoid of emission to obtain an average background value per pixel. This value was then multiplied by the aperture area measured by IRAF and subtracted from the photometric value of the source. Also, local extinction of the background will result in over-subtraction of the background on the source. This over subtraction is greatest in IRAC channels 3 and 4 where the background interstellar medium (ISM) and zodiacal light emission are highest.

We measured the flux within 1000 and 10000 AU aperture radii centered on the position of L1527; $\alpha = 04:39:53.9$ $\delta = +26:03.09.6$ (J2000). These apertures correspond to 6 and 60 pixel radii at a distance of 140 pc and the IRAC pixel scale of 1''/pixel. We use two apertures in our analysis because the 1000 AU aperture probes emission on small scales, dominated by the central envelope structure and the 10000 AU aperture probes emission

¹IRAF is distributed by the National Optical Astronomy Observatories, which are operated by the Association of Universities for Research in Astronomy, Inc., under cooperative agreement with the National Science Foundation.

dominated by extended scattered light in the outflow cavity. Lastly, we applied aperture corrections to our photometry using the methods of extended source calibration described on the *Spitzer Science Center* website. Photometry and aperture corrections are listed in Table 1.

For the ISO data, we used the same procedure as above, however we were only able to use apertures of 1000 ($7''.2$) and 5000 AU ($36''$) due to the limited field of view. The ISO photometry may have up to 30% errors as aperture corrections were unknown and background subtractions are uncertain.

The 2MASS photometry was performed using the same procedure as the IRAC data. The pixel size of the 2MASS detectors was $2''.0/\text{pixel}$ so our apertures were 3.57 pixels for 1000 AU and 35.7 pixels for 10000 AU.

Finally, photometry from the TIFKAM data were also taken using the method for IRAC data. The pixel size on the TIFKAM detector corresponds to $0''.2/\text{pixel}$, translating to a 35.7 pixel aperture for 1000 AU and a 357 pixel aperture for 10000AU. The data were calibrated using the faint NIR standards listed in (Hunt et al. 1998).

3. Observed Morphology

As shown in Figs. 1 and 2, L1527 exhibits bright bipolar scattered light nebulae which extend roughly 1.5 arcminutes (12600 AU) on each side of the central source. In addition to the large, bright cavities, the most striking features are the ‘neck’ and absorption lane between the reflection nebulae. The absorption lane is clearly shown in the Ks-band image (Fig. 2), having a width of $\sim 10''$ (1500 AU). The ‘neck’ becomes apparent in the IRAC images as a thin strip of emission bridging the gap between the cavities. The ‘neck’ is shown in more detail in Fig. 3.

In addition, we observe a bright source between the cavities on the ‘neck’ in the IRAC images, see Fig. 3. This feature was not detected in the TIFKAM or 2MASS observations. This source appears to be slightly extended as compared to a point source in all IRAC channels, though the surrounding nebulosity makes it difficult to be certain. We will discuss the possible nature of this object in §5.

In the MIPS $24\mu\text{m}$ images, L1527 is a point source, but at $70\mu\text{m}$ there is marginally resolved structure; L1527 appears elongated along the outflow axis, see Fig. 2. The radius of the envelope at $70\mu\text{m}$ is about $70''$ or about 10000AU. L1527 was not completely mapped at $160\mu\text{m}$, but we again observe extension along the outflow axis. Also, we estimate that

the L1527 envelope has a radius of approximately $100''$ or 14000 AU from the $160\mu\text{m}$ image.

While the bipolar nebulae of L1527 may in general seem prototypical and simple to model, in reality L1527 is very complex. We noticed that in IRAC Channels 1 and 2 there is an inherent lumpiness to the scattered light cavities presumably from substructure in the cavity walls; the substructure becomes unresolved in IRAC channels 3 and 4. In addition to the lumpiness of the scattered light, L1527 shows several asymmetries in brightness and geometry.

3.1. Asymmetry

The position angle (PA) of the outflow from L1527 is $\sim 90^\circ$ east of north (Zhou et al. 1996; Hogerheijde et al. 1998). Also, we observe faint Herbig-Haro objects at $\sim 230''$ west and $\sim 160''$ east of L1527 in the IRAC images (Fig. 4); they are consistent with a PA of $\sim 90^\circ$. Using this PA as the symmetry axis for the outflow cavities, there is clear asymmetry which is quite plain in Figs. 1 and 2. The southeast side of the cavity opens wider than the northeast and vice versa. Also, the cavity has an azimuthal brightness asymmetry. In the east side cavity, the south side is brighter than the north side and in the west side cavity the north side is brighter than the south side. The asymmetry seems to be a global effect on the entire envelope since the departures from spherical symmetry are observed to be qualitatively point symmetric. Also, the asymmetry appears to be present at many different wavelengths, even in the submillimeter images, see Fig. 5. The submillimeter contours are overall boxy in shape. In the southeast and northwest of Fig. 5, the contours are more extended than the northeast and southwest contours, looking like a parallelogram.

3.2. Variability

We observe the cavities of L1527 to have substantial brightness variations over time. Comparing the two epochs of observations in Fig. 6, we can see that both sides of the cavity exhibit independent variability over the entire cavity. In 2004 the western cavity was much brighter than in 2005; and in 2004 the eastern cavity is fainter than in 2005.

Fig. 7 shows the flux averaged over sectors of annuli spaced radially for each epoch. The variation between the two epochs is not large enough to affect modeling and the brightness of the cavities is fairly flat close to the center. The flatness is the result of the curved cavity shape; the distance of the cavity wall to the illuminating source changes slowly in this region. Also, at a radial distance of greater than $10''$ the cavity brightness falls off roughly

$\propto R^{-2}$ in both epochs, consistent with scattered light from a central point source incident on an optically thick wall (Whitney & Hartmann 1993). The bump at about $30''$ is due to a brightened cavity feature present in both cavities at this distance. IRAC Channels 1 and 2 are very similar in their ratios over the entire measured region, see Fig. 6. IRAC Channels 3 and 4 are similar out to about 50 arcseconds; where the scattered light falls off in these channels. IRAC channels 3 and 4 are not shown in Fig. 6 as the divided images are very noisy.

3.3. Local Extinction

3.3.1. $8\mu m$ Absorption

With the data from *Spitzer*, we are not only observing the envelope structure through scattered light, we also directly probe the envelope structure in absorption at $8\mu m$. IRAC Channel 4 is the widest IRAC band with a bandwidth of $2.93\mu m$, extending from 6.44 to $9.38\mu m$, overlapping with the $6.85\mu m$ organic ice, $9.0\mu m$ ammonia ice, and most importantly the $9.7\mu m$ silicate feature. The presence of these absorption features in IRAC Channel 4 and a significant interstellar background make it an ideal band to observe MIR extinction. Observing absorption in the MIR is not new, this type of analysis has been performed extensively on infrared dark clouds located in the galactic midplane (e.g. Simon et al. 2006; Ragan et al. 2006). Also, Looney et al. (2007) observed L1157 to have a flattened envelope in $8\mu m$ absorption.

To turn our IRAC $8.0\mu m$ image into an optical depth image, we first subtracted the estimated zodiacal light; a model calculated value is found in the image header. Then we measure the residual background emission, using the same method we used for the photometry background measurement. The $8.0\mu m$ image is then divided by the background measurement and the natural log of each pixel is calculated, yielding an optical depth image. This method assumes a constant background which may not be a realistic assumption. However, given the low S/N of the background and small angular size of L1527, modeling of the background as described in Simon et al. (2006), would not improve the analysis.

Fig. 4 shows the $8\mu m$ optical depth contours overlaid on the IRAC $8.0\mu m$ image. In addition to the asymmetries observed in scattered light, the $8.0\mu m$ absorption is asymmetric. The north side of the envelope has significantly more optical depth and covers a larger area than the south. This observation infers that there is more material to the north in our line of sight, in agreement with submillimeter observations shown in Fig. 5. The submillimeter contours are more extended on the north side of L1527 by about 20 to $30''$ than on the south

side.

Using these optical depth data, we can get a rough idea of the amount of material in the envelope. Assuming the $8.0\mu\text{m}$ opacity from Li & Draine (2001) we derive a mass of $0.22 M_{\odot}$. The measured mass is low compared to previous estimates of $2.4 M_{\odot}$ to $0.8 M_{\odot}$ from ammonia and dust emission (Benson & Myers 1989; Shirley et al. 2000; Motte & André 2001). However, there are large uncertainties in the opacity (emissivity) in the MIR and at long wavelengths. Also, the level of residual zodiacal light contamination of the IRAC images is uncertain and in general our measurement is uncertain due to low S/N of the background. The measurement is also at best a lower limit as scattered light emission is present over roughly half the envelope masking some of the extinction.

3.3.2. *Inclination Dependent Extinction*

Radiative transfer models (Whitney et al. 2003b) and simple geometry show that the local extinction of the outflow cavity lobes will depend on line of sight inclination. Local extinction refers to self-extinction by the envelope, not the ambient molecular cloud. With constant illumination of a spherically symmetric envelope, the blue-shifted outflow cavity (tilted toward the observer) should appear brighter than the red-shifted cavity (tilted away). The blue and red-shifted cavities are determined from observations of rotational transitions of molecules at submillimeter and millimeter wavelengths, e.g. CO, SiO, HCN, etc. For L1527, the eastern cavity is blue-shifted and the western cavity is red-shifted (Zhou et al. 1996; Bontemps et al. 1996; Ohashi et al. 1997; Hogerheijde et al. 1998). There is some overlap in the velocity channels indicating that L1527 is observed close to edge-on.

In the Ks-band image from TIFKAM, both the blue and red-shifted cavities are visible. However, the blue-shifted cavity is brighter by about a factor of 2 in some regions. 2MASS observations only show the blue-shifted cavity. In the two epochs of IRAC observation, the cavities have appeared roughly equal in brightness in the 2005 epoch, and the blue-shifted cavity being brighter in the 2004 epoch. These observations are consistent with dependence of cavity brightness on inclination highlighted in (Whitney et al. 2003b), indicating that L1527 is close to edge-on but slightly inclined.

This investigation of the observed morphology yields many observational constraints which were necessary to take into account while constructing our model. Some constraints such as observing L1527 nearly edge-on greatly helps modeling by reducing several degrees of freedom for opening angle and inclination. The variability does not greatly hinder the modeling effort since the overall morphology of the object remains constant and the overall

increase or decrease in intensity is at most a factor of 2. Finally, reproducing the observed central source and dark lane requires specific attention in constructing a model of L1527.

4. Modeling

4.1. Envelope and Disk Structure

To interpret the observations, we used the radiative transfer code of Whitney et al. (2003a) to construct a model of the L1527 data. This code uses the Monte Carlo method to calculate radiative equilibrium and include multiple scattering. The model has many parameters to tune, some more important than others; we will review the parameters important to our study.

We model the central protostar with a stellar atmosphere for a given effective temperature and radius. In addition to the protostellar luminosity, we found that we needed strong disk emission. The strong disk emission can come from high accretion luminosity, a bright star illuminating the disk, or a combination of both.

We assume the typical model for T Tauri accretion in which material from the inner disk falls along magnetic field lines onto the protostar creating an accretion shock which is assumed to radiate as a blackbody over an area of 0.01 of the stellar surface (Calvet & Gullbring 1998). In addition to heating the envelope, emission from this accretion shock heats the disk along with the radiation from the stellar photosphere. Local viscous dissipation also heats the disk, but the dominant disk heating is the protostar plus accretion shock irradiation. These disk heating mechanisms combined result in the disk emitting substantial NIR to MIR radiation.

The total system luminosity is

$$L_{total} = L_* + L_{shock} + L_{disk}, \quad (1)$$

where L_{shock} is the luminosity of the accretion shock on the star,

$$L_{shock} = \frac{GM_*\dot{M}_{disk}}{R_*} \left(1 - \frac{R_*}{R_m}\right) \quad (2)$$

and L_{disk} is the luminosity from viscous energy release,

$$L_{disk} = \frac{GM_*\dot{M}_{disk}}{R_{in}}. \quad (3)$$

In these equations, M_* is the central source mass, \dot{M}_{disk} is the disk accretion rate of the disk onto the star, R_{in} is the inner radius of the disk, generally the dust destruction radius where

the dusty disk is truncated, and R_m is the magnetospheric truncation radius. In reality, the disk extends to R_m ; the disk inside the dust destruction radius R_{dd} is composed of dust-free gas which may be optically thin or thick. Currently, there are few observational constraints on the properties of the inner disk; thus, it is not included in as an energy source in the model. The gaseous inner disk may be an important detail that our model lacks.

The disk structure is assumed to be a standard flared accretion disk structure (e.g. Hartmann 1998) with a density profile given by

$$\rho(r) = \rho_0 \left(1 - \left(\frac{R_*}{r} \right)^{1/2} \right) \left(\frac{R_*}{r} \right)^\alpha \exp \left[-\frac{1}{2} \left(\frac{z}{h(r)} \right)^2 \right] \quad (4)$$

where r is the radial coordinate of the disk, and $h(r) = h_0(r/R_*)^\beta$. The model does not assume any temperature structure for the disk *a priori* thus the $h(r)$ is not calculated self-consistently throughout the disk. The model solves the hydrostatic equilibrium equation to obtain the scale height $h(r)$ at the dust destruction radius, modified by the flaring power-law β , for the entire disk structure. However, to ensure we model parameters that are roughly physically consistent, we manually specify a scale height for the model determined from the scale height at the dust destruction radius

$$h_{dd} = \left(\frac{kT_{dd}R_{dd}^3}{GM_*\mu m_p} \right)^{1/2} \quad (5)$$

where T_{dd} is the dust destruction temperature, 1400K, μ is the atomic mass unit assumed to be 2, m_p is the mass of a proton, k is the Boltzmann constant, and R_{dd} is the dust destruction radius given by

$$R_{dd} = \left(\frac{T_{eff}}{T_{dd}} \right)^{2.1}. \quad (6)$$

T_{eff} refers to the effective temperature of the star, including the accretion luminosity. The code states that the power 2.1 comes from an empirical fit, if the wall and star were in equilibrium and assuming perfect blackbody radiation, the power should be 2.

For the circumstellar envelope, we assume a TSC envelope with the density structure given by

$$\rho(r) = \frac{\dot{M}_{env}}{4\pi(GM_*r^3)^{1/2}} \left(1 + \frac{\mu}{\mu_o} \right) \left(\frac{\mu}{\mu_o} + \frac{2\mu_o^2 R_c}{r} \right)^{-1}. \quad (7)$$

\dot{M}_{env} is the mass infall rate of the envelope onto the disk, R_c is the centrifugal radius where rotation becomes important, $\mu = \cos \theta$, and μ_o is the cosine polar angle of a streamline out to $r \rightarrow \infty$. Inside of R_c ; $\rho_{env} \propto r^{-1/2}$ and outside R_c ; $\rho_{env} \propto r^{-3/2}$. The centrifugal radius controls the optical depth to the center of the envelope, increasing R_c decreases the overall

envelope density. The overall mass of the envelope does not strongly depend on R_c as the centrifugal radius is generally small compared to the outer envelope radius.

Bipolar cavities in the envelope are obviously required to fit the observations of extended scattered light and thermal emission. These bipolar cavities extend from the central protostar to the outer radius of the envelope. Curved or streamline cavities were options in modeling, we adopted curved cavities as they allowed for greater flexibility in modifying the cavity shape. The curved cavity structure is defined by $z = C(x^2 + y^2)^{b/2}$, where C is a constant determined by a relation between the cavity opening angle and envelope radius, and b is the shape parameter, the power of the polynomial defining the cavity shape. In our model, it was necessary to use two cavities of different sizes in the inner and outer envelopes. The cavity structure will be discussed further in §5.

Table 2 lists the parameters of the model we found to best fit L1527. The stellar parameters are uncertain and were simply taken to be those of typical Taurus T Tauri stars and were not varied. The total system luminosity (star plus disk accretion) is very important, depending on both the fixed stellar and the accretion disk parameters. There are several parameters for the accretion disk, but in terms of the modeling, the most important ones are the disk accretion rate, which sets the disk and accretion shock luminosity, and scale height specifying the inner disk “wall” at the dust destruction radius, which dominates the emission in the IRAC bands (see §5). The other disk parameters are relatively unimportant. The envelope infall rate in conjunction with the assumed stellar mass set overall optical depth of the envelope and the amount of long-wavelength thermal emission. The cavity properties are somewhat arbitrary but are simply tuned to match the observed morphology. The inclination angle is essentially edge-on, and the cavity and ambient densities, sometimes used in other modeling, are set to zero in our investigation.

4.2. Dust Properties

The default envelope dust properties assumed in the model are $R_V = 4$ dust grains with 5% H_2O ice coatings. This is one of the standard dust opacity tables included with the Whitney et al. (2003a) model which is derived from Kim et al. (1994). These dust properties are intended to be similar to the ISM dust in Taurus. These dust grains do not include the $6.0\mu m$ H_2O , $6.85\mu m$ CH_3OH , and $15.2\mu m$ CO_2 ice features; we observe all these ice features typically in Class 0 and Class I protostars (F07).

The dust properties are a source of uncertainty in the model. Dust grain models appropriate for the ISM may not be appropriate for Class 0 envelopes. If dust grains in the

diffuse ISM of Taurus are able to develop ice coatings (Whittet et al. 2001) and grow in dense regions (Flaherty et al. 2007; Román-Zúñiga et al. 2007), this leads to the possibility that considerable grain growth could occur in dense protostellar envelopes. Larger grains would have higher albedo out to longer wavelengths and could help to explain the intensity of the observed scattered light in the MIR.

Driven by our observations, we have constructed a dust model which uses larger dust grains than a standard ISM dust model. The dust model is calculated using the method described in D’Alessio et al. (2001), with additional optical constants for graphite from Draine & Lee (1984). The grain size distribution is defined by a power law grain size distribution $n(a) \propto a^{-3.5}$, with $a_{min} = 0.005\mu\text{m}$ and $a_{max} = 1.0\mu\text{m}$. We used dust grains composed of graphite $\zeta_{graph} = 0.0025$, silicates $\zeta_{sil} = 0.004$, and water ice $\zeta_{ice} = 0.0005$; abundances are mass fractions relative to gas. The given abundances infer a gas to dust ratio of 133. Our dust model does not include organic molecules, all carbon is in the form of graphite, nor does it include the additional ice features detailed at the start of this section. Dust grains larger than $a_{max} = 1.0\mu\text{m}$ would have too much albedo long-ward of $8.0\mu\text{m}$ yielding significant extended emission between $8.0\mu\text{m}$ and $15\mu\text{m}$. Observations by ISO do not show significant extended emission above the background at 9.6 or $11.3\mu\text{m}$. These observations constrain the maximum possible size of dust grains in the outer envelope of L1527 to be $\sim 1\mu\text{m}$ in radius. The opacity and albedo curves of our assumed dust model is plotted against an ISM dust model (Kim et al. 1994) in Fig. 8.

4.3. Model Fitting

Due to the inherent uncertainties in modeling L1527 and observed asymmetries, we did not quantitatively fit our images or SEDs using a χ^2 or equivalent minimization routine. To fit the observed morphology of the image, we convolved the model image with the appropriate, instrument specific, PSF and compared it to the observed data. If an image looked similar we noted the particular parameter set and ran the model again with more photons to obtain a higher S/N image. We cannot duplicate the asymmetric cavities of L1527, due to the axisymmetry of the model, but the general morphology modeled is quite similar.

With the high S/N images, we compared the intensity averaged over sectors radially spaced (Fig. 9) to compare the data and the models. In Fig. 9 we see that the $3.6\mu\text{m}$ channel agrees the best while the overall strength of the scattered light in the 4.5 , 5.8 and $8.0\mu\text{m}$ channels falls short at all radii, though the shape of the curves is quite similar. At Ks-band, the model also roughly agrees with the observations. Similar to the IRAC data, the Ks-band plot also has the bump at $30''$, probably due to a bright spot in the cavity or

an outflow knot. In addition, the intensity of the modeled central object in the IRAC bands does roughly agree with the observations.

The SED fitting was done by eye, adjusting the luminosity controlling parameters until the model was as close to the observed SED as possible. We were able to nearly bring the overall SED of the model and observations into agreement. Also, the asymmetry of the cavities does account for some of the discrepancy between the model and observed SED in the 10000 AU aperture. Also, we apply a foreground extinction of $A_V = 3$ to the SED and images for fitting. The addition of extinction extinguishes the extended scattered light the model predicts in the visible while hardly affecting the portion of the SED we are fitting. The extinction toward L1527 is uncertain since it is a protostar embedded within a dark cloud. However, the assumed extinction is not atypical for Taurus.

5. Results

In order to match the observed morphology of L1527, changes to the standard Whitney et al. (2003a) model were necessary. The largest necessary change was to the bipolar cavity configuration. Here we describe the changes to the standard parameter set of the model and review the resulting physical parameters and their significance.

5.1. Reproducing the Scattered Light Morphology

At the start of our modeling effort we adopted the parameters fit by F07; see Table 2. We soon found that we could not replicate the dark lane, ‘neck’, or central object with the standard bipolar cavity geometry of the model and a relatively flat disk. In Fig. 12 we show how the model looks using the default, single cavity structure. These images do show a dark lane, however it is very thin, and there is no central source in the IRAC images. The appearance of this dark lane is similar to those observed by Padgett et al. (1999), which are the relatively thin shadows of dusty circumstellar disks. The thickness of the dark lane in L1527 requires an structure that is as wide as it is thick, unlike a disk. We thus concluded that the observed dark lane and ‘neck’ must be due to the envelope structure and the standard bipolar cavities of the model would not suffice.

To reproduce the observed ‘neck’ morphology we used an inner, narrow outflow cavity with an offset outer outflow cavity; this ‘dual-cavity’ geometry is shown schematically in Fig. 10. In Fig. 3, we compare the results of this model convolved with the IRAC PSF to the 3.6 μm IRAC image. Then in the bottom panel of Fig. 3, we show how the modeled

central source actually appears at high resolution. The bright emission ridges in the IRAC images are produced at the base of the outer cavity; the inner cavity offsets the outer cavity, producing neck absorption while still transmitting enough scattered light to form the central source. The dual-cavity model has some direct support in the image; as shown in the upper left panel of Fig. 3, the scattered light cavity appears much narrower near the source, especially on the western side. Possible physical motivations for the envelope structure we have created are discussed in §6.

In order to match the morphology of L1527 using the dual-cavity structure, the opening angle and cavity shape parameter are relatively well constrained. As discussed in §4 the cavities we model are defined by a polynomial of a variable degree; we refer to the polynomial degree as the shape parameter. The shape parameter determines how quickly the cavity widens in the inner envelope. The cavity offset is associated with the inner/outer cavity opening angles and shape parameters. Our best fitting outer cavity offset is 100 AU, a larger offset creates a central source that is too resolved. A smaller offset creates an unresolved central source.

The opening angle of the outflow cavities is defined as the angle measured from the center of the envelope to the outer envelope radius. Thus, near the center of the envelope, the cavity opens wider than the opening angle defined. The opening angle of the outer cavity is modeled to be 20° and the inner cavity opening angle is modeled to be 15° . The inner cavity is modeled to have a shape parameter $b = 1.5$ and the outer cavity has a shape parameter $b = 1.9$. We need to model the outer cavity to have a shape parameter such that it opens wide a short distance from the envelope center. The inner cavity then casts a shadow on the widely opening outer cavity, and creates the apparent central point source in scattered light. The shape parameters for the cavities are empirical. We adjusted the inner and outer shape parameters and opening angles until the models appeared similar to the observations. In the end, the morphology of the scattered light in the modeled cavities is similar to the observations.

The scattered light in our model and observations require a large envelope. To match the scattered light profile in Fig. 9 and extent of scattered light in the images, it was necessary to use an envelope with a 15000 AU outer radius. Larger radii give too much optical depth to the center of the envelope. With smaller radii, the scattered light ends prematurely. In addition to the outer radius, the overall optical depth greatly depends on R_c , \dot{M}_{env} , and M_* . We assume that the central protostar has a mass of $0.5M_\odot$, however this is an unknown. The best \dot{M}_{env} that we were able to fit is $1.0 \times 10^{-5} M_\odot \text{ yr}^{-1}$. KCH93 alternatively express

the infall rate as

$$\rho_1 = 5.13 \times 10^{-14} \left(\frac{\dot{M}_{env}}{10^{-5} M_{\odot} yr^{-1}} \right) \left(\frac{M_*}{1 M_{\odot}} \right)^{-1/2}. \quad (8)$$

For our \dot{M}_{env} and M_* , we find $\rho_1 = 3.75 \times 10^{-14} \text{ g cm}^{-3}$; corresponding to a dense circumstellar envelope appropriate for modeling a Class 0 or I object. A Class 0 object is expected to have a small R_c and high \dot{M}_{env} .

For the outer disk radius we also use the same value as R_c , it is generally accepted that the disk will form inside the centrifugal radius. Outside R_c , the angular momentum is not great enough to prevent infall. The value of R_c we model must be smaller than the outer cavity offset in order to create the shadowing effect due to the control R_c has on the optical depth. The best fitting R_c that we model is 75 AU.

Modeling the inclination of L1527 was trivial as it is observed to be nearly edge-on. An inclination of 85° agrees well with the observations; an inclination much lower than 80° blends the inner cavity scattered light with that of the outer cavity.

5.2. SED Fitting: Disk Emission

The fundamental constraint that we need to model is the total system luminosity. Integrating over all available photometric data points, we measure a bolometric luminosity (L_{bol}) of $1.97 L_{\odot}$. The L_{bol} gives an observational constraint on the total system luminosity that we are modeling. Our measured L_{bol} is consistent with the recent estimate of $1.9 L_{\odot}$ by F07. L_{bol} is probably a lower limit on the total luminosity because the object is observed edge-on and some radiation from the central protostar may escape through the outflow cavity without scattering or reprocessing. However, it is unlikely that the true luminosity is vastly larger because the outflow cavities do not span a large solid angle as seen from the source; thus most of the central source emission should be absorbed and reemitted by the envelope.

The central protostar is chosen to be a $1 L_{\odot}$ star with an effective temperature of 4000K, a radius of $2.09 R_{\odot}$, and a mass of $0.5 M_{\odot}$. These stellar parameters are chosen from the stellar birthline of a typical T Tauri star (Hartmann 1998) as an estimate for the properties of the central protostar. These parameters are an assumption, observations do not constrain the central source. Though we know L1527 is probably a binary (Loinard et al. 2002), we do not attempt to model multiple stars and/or disks. Doing so would have increased complexity and essentially just given us a free parameter as there are no constraints on the binary pair, other than projected separation.

The brightness of the scattered light combined with an approximate limit on the bolo-

metric luminosity makes it impossible to explain the observations without a dominant contribution from the circumstellar disk at IRAC wavelengths. For plausible parameters, the infrared emission of the central protostar is much too faint for a given total luminosity. We require a much redder central source SED, with a high proportion of the luminosity being emitted in the NIR to MIR, in order to explain the observations.

For the fixed protostellar parameters, our best results required an accretion luminosity of $\sim 1.6 L_{\odot}$ corresponding to a disk accretion rate of $3.0 \times 10^{-7} M_{\odot} \text{ yr}^{-1}$, so that the true bolometric luminosity in our model is $\sim 2.6 L_{\odot}$. Most of this accretion luminosity is radiated in the optical to ultraviolet by the accretion shock. Both the star and the accretion shock heat the disk, producing the NIR to MIR emission. This irradiation heating of the disk dominates the local viscous dissipation and so the total luminosity, star plus accretion shock, is the important parameter. Thus in principle we could either make the star fainter and allow the accretion shock to emit essentially all the radiation; conversely, we could reduce the disk accretion rate by making the central star brighter, such that the total luminosity remains constant. Thus, our model results in an upper limit to the accretion luminosity and hence an approximate limit to the disk accretion rate of order $5 \times 10^{-7} M_{\odot} \text{ yr}^{-1}$. This disk accretion rate is fairly high compared to most Class II objects which accrete about $10^{-8} M_{\odot} \text{ yr}^{-1}$. However, we cannot distinguish between stellar and accretion luminosity with the model. Though, significant accretion makes sense in the case of a young protostar.

With the limitations on the bolometric luminosity it was difficult to produce enough scattered light in the IRAC bands. Most of the radiation at these wavelengths comes from the inner disk “wall”, i.e. the inner edge of the disk where dust is evaporated (e.g. Dullemond et al. 2001; Tuthill et al. 2001; Muzerolle et al. 2003). In our model, this inner disk region emits at about 1400 K, the dust destruction temperature. The total luminosity thus depends upon the wall height, and, in our case, strongly upon the disk wall geometry. With our assumed stellar and accretion luminosity, the dust destruction radius is ($14.25 R_{*}$, 0.139 AU). The disk is modeled with a scale height $h(100\text{AU}) = 10.52\text{AU}$ with a flaring power of $\beta = 1.125$ and a radial density exponent $\alpha = -2.125$. The scale height is calculated using Equation 5. The total disk thickness at R_{dd} is about 0.12 AU.

Even with this bright inner disk wall, we still needed to produce more NIR to MIR photons in the disk. In particular, our initial assumption that the disk wall is vertical meant that many wall photons were not emitted toward the poles, where we need them. We have modified the inner disk wall to resemble the inner disk structure calculated by Tannirkulam et al. (2007), which creates a wedge-shaped wall resulting from dust settling (D’Alessio et al. 2006). The wedge-shaped inner disk wall will emit optically thick radiation with a temperature distribution as determined by the radiation transfer. This wedge struc-

ture will emit more NIR and MIR radiation toward the poles, into the outflow cavity, than the vertical wall. The central star plus disk spectrum as observed pole-on is shown in Fig. 11 as the dotted line. The central star plus disk spectrum has a very strong NIR to MIR excess making the spectrum very flat from visible to mid infrared wavelengths.

Despite the extraordinary lengths that we have taken to get more NIR to MIR light out of our model, we still fall short by about a factor of two at large spatial scales in IRAC channels 1 - 3. It may be that complex structure in the cavity walls, seen in the real object as bright spots, accounts for the difference. An alternate way to increase the scattered light flux is to include dust in the outflow cavity. This would scatter some of the light from the central protostar and disk that would otherwise escape. However, it is not clear whether dust grains would condense in the evacuated outflow cavity. We experimented with including dust in the outflow cavity and found that the shadow cast by the inner cavity is washed out if there is dust in the cavity near the central object, where we would expect dust grains to possibly condense.

Even with the difficulties in constructing a model of L1527, our end result well approximates the observed morphology in the infrared images (Fig. 13a,b), IRS spectrum, and SED (Fig. 11). Though we did not directly fit the submillimeter observations of L1527, our model image at $850\mu\text{m}$ does approximate the observed morphology (Fig. 5). Fitting the observed details in the image are as important as fitting the spectrum itself.

Fig. 12 shows how the L1527 model looks using only a single cavity. Comparison to Fig. 13a,b illustrates the benefits of the dual-cavity model in the case of L1527. The single-cavity images in Fig. 12 fail to produce the thick dark lane and central source between the outflow cavities with the same parameters as the dual-cavity model. Thus we have concluded that L1527 is probably not represented by simple bipolar cavities carved from a TSC envelope.

6. Discussion

6.1. Comparison to Previous Models

The first attempt at modeling L1527 was done by KCH93. This study used simple TSC envelopes without cavities to model the spectrum of many Class 0 and Class I sources in Taurus. KCH93 modeled fixed outer radii of 3000 AU while varying luminosity, envelope density, centrifugal radius, and inclination. For L1527, KCH93 modeled greatly larger values of envelope density $\rho_1 = 3.16 \times 10^{-13} \text{ g cm}^{-3}$ compared to our value of $\rho_1 = 3.75 \times 10^{-14} \text{ g cm}^{-3}$ and $R_c = 300 \text{ AU}$ versus our value of $R_c = 75 \text{ AU}$. The high envelope density modeled by KCH93 is partially explained by the larger R_c ; a large R_c decreases the optical depth

to the envelope center. The luminosity of $1.3 L_{\odot}$ modeled by KCH93 is somewhat lower than our value of $2.6 L_{\odot}$. The differences are likely due to the different modeling techniques and less long wavelength photometry in KCH93. Also, our modeled inclination of $\sim 85^{\circ}$ is within their estimated range of $60-90^{\circ}$; see Table 2 for a comparison between KCH93 and our modeled parameters. The differences in our modeled envelope parameters and those of KCH93 may be due to the absence of outflow cavities in the KCH93 models as well as differences in abundances assumed for the dust models. The large R_c modeled by KCH93 is necessary to fit the NIR photometry without including cavities.

F07 also modeled L1527 by SED fitting of multi-wavelength photometry and the IRS spectrum. This study uses a recent revision of the model used in KCH93, with outflow cavities. Many of the physical parameters modeled are similar to our results while some differ. The envelope density, $\rho_1 = 1.00 \times 10^{-14} \text{ g cm}^{-3}$ differs from our value of $\rho_1 = 3.75 \times 10^{-14} \text{ g cm}^{-3}$. Also, the modeled envelope radius is similar, 10000 AU compared to our value of 15000 AU. Additionally, the luminosity modeled by F07 was $1.8 L_{\odot}$, slightly less than our value of $2.6 L_{\odot}$. A limitation of the F07 model is that there is no way to define an aperture to compare the small and large scale emission. The model works fine for the $10-50 \mu\text{m}$ range in wavelength if all the flux comes from small scales, see Fig. 11. However, for $\lambda < 10 \mu\text{m}$ and $\lambda > 100 \mu\text{m}$ the amount of flux measured can vary greatly depending on the aperture. Despite the aperture limitations, the model results are meaningful as the wavelength range of the IRS spectrum is not sensitive to aperture and the spectrum is fit quite well. See Table 2 for a comparison of all modeled parameters.

In a recent study employing the Whitney et al. (2003a) model, R07 fit L1527 photometry from IRAC, MIPS, and IRAS against a grid of 200,000 model SEDs. These envelope models are based on the standard bipolar cavity structure of the Whitney et al. (2003a) model as described in §4. The fits of this model grid seem to vary depending on the method of fitting. The models which fit SEDs using the total integrated flux an entire object are consistent with our results. However, the parameters derived from their resolved source analysis of L1527 are mostly inconsistent with our results. This analysis used multiple apertures to examine the integrated flux on small to large scales. We can account for this inconsistency by observing that their best fitting models greatly overestimate the long wavelength SED. This is because the luminosities modeled by R07 are 155 and $20 L_{\odot}$, much larger than our modeled luminosity of $2.6 L_{\odot}$ and the measured L_{bol} of $\sim 2 L_{\odot}$. The very high luminosities modeled probably result from the lack of a strong NIR to MIR excess from the disk and improper weighting of the far-infrared photometry. The central protostar is modeled to be the primary source of scattered light photons. In our models, the NIR to MIR scattered light comes from a combination of accretion and the inner disk wall. Also, the R07 analysis did not apply aperture corrections to IRAC channels 3 and 4. Those channels have correction factors

less than 1 for apertures larger than $10''$. In addition to high luminosities, R07 modeled high envelope densities, $\rho_1 = 2.81 \times 10^{-12}$ and $8.77 \times 10^{-13} \text{ g cm}^{-3}$ compared to our density of $\rho_1 = 3.75 \times 10^{-14} \text{ g cm}^{-3}$. The high envelope densities are necessary to extinct the high stellar luminosity. Also, the lack of an envelope structure to create the central object in the R07 models makes it difficult to fit the small and large scale IRAC fluxes simultaneously with reasonable parameters.

6.2. Envelope Neck

To fit the SED and image of L1527 in multiple apertures at all wavelengths, we found it necessary to introduce a new type of outflow cavity structure. We are limited by axisymmetry in the Whitney et al. (2003a) model in ways to create the observed central object and separated cavities. Our model may be an axisymmetric approximation to a more complex structure. Having discussed the morphological reasons for adopting the ‘dual-cavity’ structure in §5, we now review the physical motivations for such a structure.

Delamarter et al. (2000) created MHD simulations of protostellar outflows originating from a spherical wind driven by the central protostar. The density structure assumed for the envelope was the parametrization of the TSC model for the collapse of a flattened sheet (Hartmann et al. 1996) interacting with a spherically-symmetric outflow. The enhanced density at the equator of the infalling material resulted in higher ram pressure working against the ram pressure of the wind, creating a kind of ‘neck’ structure. Our TSC model does not have an enhanced equatorial density as in the Delamarter et al. (2000) model. However, Ohashi et al. (1997) observe a dense, possibly rotating, inner envelope toroid in L1527 with interferometric C^{18}O observations. Alternatively, one might suppose that the ram pressure of the wind varies from the axis in such a way to produce a ‘neck’, with weaker flow near the equator than the poles; the effect would be similar because the relevant quantity is the ratio of wind to inflow ram pressures, not the absolute values. As outflows are clearly collimated, with high-density jets along the axis, this supposition is physically plausible.

It is also worth noting that the ‘neck’ region of L1527 is not axisymmetric. A precessing jet (Gueth et al. 1996; Ybarra et al. 2006) could partially evacuate the polar regions allowing the spherical outflow to expand, creating a wider outflow cavity with a standard TSC envelope.

Another possibility is that binary accretion patterns are responsible for the observed morphology. Figs. 1 and 2 of Bate & Bonnell (1997) show that proto-binary stars create an evacuated inner region of the protostellar envelope, with streams of material falling in

at particular longitudes. Thus, the ‘neck’ might be related to these streams and evacuated region, while the outer cavity is dominated by the outflow interacting with a more axisymmetric envelope. It is worth considering this further as L1527 appears to be a binary system (Loinard et al. 2002).

6.3. Variability and Asymmetry

In addition to possibly causing asymmetry in the overall structure, binary interactions could contribute to the variability observed in L1527. As described in §3 the variability seems to affect each cavity lobe independently. Both cavities vary in brightness but one becomes fainter as the other becomes brighter. The variability is consistent with the scattered light from a central source; the light travel time out to the edges of the observed scattered light image is ~ 0.25 years and observations were almost a year apart.

Resolved observations of the HH30 disk have shown substantial variability over the past 15 years (Watson & Stapelfeldt 2007). The mechanism behind these variations is uncertain but it is conjectured that inner disk warps caused by a companion, accretion shocks unevenly heating the disk, and/or binary interactions could be causing uneven patterns of illumination. These proposed mechanisms may cause selective illumination of different parts of the cavity from the disk since most NIR to MIR photons come from the disk. We may be observing the effects on the envelope of a process similar to the variability in the disk of HH30.

Variability of the scattered light intensity is not unexpected since we know Class 0 objects are still accreting material and our models require high accretion and infall rates. The variability is easier to understand if the disk accretion luminosity is large, as we have modeled it to be. T Tauri stars which show the most variation are most commonly accreting systems.

In §3 we described the azimuthal asymmetry of L1527; the brightness difference of the north and south sides of the cavities. The radiative transfer study by Wood et al. (2001) showed that misaligned circumstellar disks could cause asymmetric illumination of the outflow cavities in the radial and azimuthal directions. In the case of T Tau, Fig. 2 of Wood et al. (2001) shows that one side of the cavity could be significantly more illuminated than the other, similar to what we observe in L1527. The contoured IRAC and Ks-band images of L1527 in Fig. 13a clearly show the azimuthal asymmetry of L1527. Individual circumstellar disks around the central binary (Loinard et al. 2002) could be producing the observed brightness asymmetries.

We noted in §3 that even the submillimeter image shows asymmetry, see Fig. 5. The

boxy contours are extended along the outflow axis, probably due to the heating along the outflow cavity walls and possibly dust in the cavity; the contours should be round without a cavity present. The contours are more extended in the southeast and northwest, indicating asymmetric heating in the same locations as asymmetric scattered light suggesting that they are related.

6.4. Interpretation of Physical Parameters

In §5 we described the physical parameters of the model we have constructed. Two of the most important parameters derived in our modeling are the mass infall rate \dot{M}_{env} and the mass accretion rate \dot{M}_{acc} . Assuming a central stellar mass of $0.5 M_{\odot}$, we model a \dot{M}_{acc} of $3 \times 10^{-7} M_{\odot} \text{ yr}^{-1}$, an order of magnitude larger than a typical T Tauri star for which $\dot{M}_{acc} \sim 10^{-8} M_{\odot} \text{ yr}^{-1}$. Our high \dot{M}_{acc} modeled is further supported by the strong forbidden optical emission lines (i.e. [OI], [NII], [SII]) and Hydrogen alpha observed by Eiroa et al. (1994) and Kenyon et al. (1998); these observations infer high disk accretion rates as well as jet emission.

In our model, \dot{M}_{env} is about two orders of magnitude larger than \dot{M}_{acc} , which means that the disk is rapidly building up mass since it cannot pump material onto the star quickly enough. Thus the disk will either get very massive in a short period of time or the excess mass is expelled by the outflow. Also, the widening of the outflow cavities may be working to quench the mass infall, not enabling the disk to gain a very large final mass (Arce & Sargent 2006).

With our best fitting \dot{M}_{env} , similarly ρ_1 which we get from our assumed stellar mass, we get an envelope with a density similar to that of many Class I objects as modeled by F07. While the envelope of L1527 is not substantially more dense than a typical Class I protostar, the envelope is substantially larger in spatial extent. We observe the very extended scattered light with IRAC, but no other Class I object in Taurus has such extended scattered light except for L1551 IRS 5 (e.g. Osorio et al. 2003) and L1551NE (Swift & Welch 2008). However, SED models by F07 fit large envelopes for most Class I sources for which we do not observe extended scattered light. This contradiction suggests that the size of the envelope may not be well constrained by SED modeling and spatially resolved observations are required to constrain this parameter.

Related to \dot{M}_{env} is the overall mass in the envelope. The mass of our best fitting model was $1.72 M_{\odot}$. This mass is comparable to the $2.4 M_{\odot}$ measured by Benson & Myers (1989) from ammonia observations. Observations of dust emission yield masses of $0.8 M_{\odot}$ from

Shirley et al. (2000), and $0.9 M_{\odot}$ from Motte & André (2001). While these measurements are low, the dust emissivity may be uncertain by a factor of 3 (Shirley et al. 2000) which could account for the difference.

Our best fitting model was not strongly dependent on the value of R_c , but it had to be less than the outer cavity offset to create the shadow effect. Our disk radius was chosen to match R_c at 75 AU, given our upper limit on R_c by the cavity offset, our disk will be small compared to the typical 200 AU size of disks as observed by Andrews & Williams (2007). This implies that disk of L1527 is still being built up and there are likely complex dynamical interactions on small scales in the inner envelope as hinted to previously.

6.5. Class 0 versus I

The Class 0 definition from Andre et al. (1993) requires that the ratio of submillimeter luminosity to the bolometric luminosity is 5×10^{-3} . This definition is not exclusive of the I through III classification of Lada (1987). A Class 0 object can also be a Class I object if there is detected emission in the NIR to MIR. *Spitzer* has revealed previously undetected MIR scattered light emission from many Class 0 protostars (Tobin et al. 2007; Seale & Looney 2008).

With the inclusion of outflow cavities in the standard envelope models, this Class 0 definition immediately becomes muddled. Using L1527 as an example, with the observed inclination, it is clearly a Class 0 object, all the power is in the long wavelength portion of the SED, see Fig. 11. However, we can predict what our L1527 model would look like at different inclinations. As L1527 is tilted toward our line of sight, we see further down the cavity through increasingly less extinction. The peak of the long wavelength SED does not change, but more power goes into shorter wavelengths. There is a point when the object no longer meets the criterion for a Class 0 object and is a typical Class I, see Fig. 14. For example, our model spectra at varying inclinations are similar in shape to the spectra of Class I protostars in Taurus from F07. Specifically, at an inclination of 63° , our model is similar to DG Tau B, at 49° it is similar to IRAS 04239+2436, and the same applies for a few others.

From the SEDs shown at various inclinations in Fig. 14, we show that L1527 may not necessarily be a Class 0 object and could be a Class I if it were oriented differently. Because Class definitions are dependent on the SED, spatially resolved observations are crucial to our understanding of protostellar structure and evolution. There are spatially resolved observations of several Class I protostars in Taurus from Padgett et al. (1999); these Class I objects

are quite different from L1527. The scattered light morphologies observed by Padgett et al. (1999) are all very small in spatial extent (~ 2000 AU) compared to L1527, which is extended over nearly 30000 AU. Without resolved observations, we would be ignorant of their inherent differences.

6.6. General Applicability of the Model

An important question must be asked of our results; is L1527 a special case in requiring a modified cavity structure to fit its morphology or are our results more generally applicable? Some protostars associated with scattered light nebulae seem to show a similar morphology to L1527; a point source located between two outflow cavities. However, not all sources have cavity structures as bright as L1527 and not all objects appear to have a cavity separation like L1527, although this may be an issue of angular resolution and inclination.

The observations by Padgett et al. (1999) appear to be consistent with a single outflow cavity model; Stark et al. (2006) modeled these objects as such. However, in contrast to L1527, these objects seem to be more evolved, Class I objects. Protostars may evolve such that a more simplified model will suffice as the infall phase is ending. The dual-cavity model may only be applicable to the very young, high mass infall phase.

Seale & Looney (2008) cataloged many remarkably bright outflow cavity structures in archived observations from the *Spitzer Space Telescope*. Several objects (IRAS 05491+0247, IRAS 18148-0440, L1251B, and others) show bright cavity structures with an apparent point source in the middle. From this catalog of scattered light nebulae observed with IRAC, it appears that the model we have developed for L1527 may be more than just a special case.

We stress that this morphology of an observed central object and separated outflow cavities for Class 0 sources is only observed between $3\mu\text{m}$ and $8\mu\text{m}$ thus far. Shorter wavelengths are too extincted to detect the central object and longer wavelengths wash out the separation because the dust is less opaque to the incident radiation. Objects with a less dense circumstellar envelope may show a central object at K-band as seen in NICMOS observations by Meakin et al. (2003) and Hartmann et al. (1999). Also, an object must be viewed nearly edge-on for this morphology to be apparent. Sources inclined much less than 80° will blend the central object with the blue-shifted outflow cavity. Though, a gap caused by the inner envelope shadowing should still be visible between the red and blue-shifted cavities.

In addition to the necessity of edge-on observation, objects also must be nearby. The central object of L1527 is only separated from the bright outflow cavity by $\sim 3''.6$. If the distance to L1527 were twice what it is, the separation may be smeared out by the PSF.

These criteria for observation of this morphology will create a selection effect; however, increased spatial resolution in the NIR to MIR is not far away and detailed modeling may be able to disentangle the inclination effects.

6.7. Dust Properties and Emission Processes

As discussed in §5, we were not able to completely model the SED with the assumed dust model. Our dust model is not unique, there could be different dust grain size distributions in different parts of the envelope; large grains in the dense inner regions and small grains in the outer regions. *Spitzer* has provided a wealth of data with which more precise dust models may be developed; most importantly, the infrared extinction law in the IRAC wavelengths has been proven to be flatter than expected (Indebetouw et al. 2005; Flaherty et al. 2007; Román-Zúñiga et al. 2007). This flat extinction law implies that grain growth has occurred in dense regions (Román-Zúñiga et al. 2007). Thus protostars start out with dust that is larger than general ISM dust. These extinction law measurements support our adoption of a larger dust grain model for our modeled envelope. The larger dust grains have significantly more albedo in the NIR to MIR.

Also, as shown in Fig. 11, the model spectrum tends to fall below most of the submillimeter data points. This trend again indicates that there are details missing from our assumed dust model. Other, more complex organics may more accurately represent an envelope dust model (e.g. Pollack et al. 1994). Also, heating of the outer envelope from the interstellar radiation field could be responsible for the observed submillimeter fluxes slightly disagreeing with the model. The upcoming *Herschel Space Telescope* will give new insights into the submillimeter properties of dust.

In addition to the scattered light emission, there is a possibility of some shock-excited molecular line emission resulting from the jets and outflows in the cavities. The strong Herbig-Haro spectrum detected in the cavity of L1527 (Eiroa et al. 1994; Kenyon et al. 1998) suggests that the outflow cavities could have some NIR to MIR emission from H_2 ro-vibrational lines. Many H_2 lines are present throughout all the IRAC bands. However, IRS observations of protostars in F07 showed no evidence for strong emission lines at IRAC wavelengths. Our narrowband H_2 ($2.12\mu m$) observations of L1527 did detect some weak emission in excess of observations with the H_2 ($2.09\mu m$) continuum filter. However, the H_2 emission is at most 8% of the total Ks-band flux which is within our errors for the flux at Ks-band and would not greatly affect modeling.

In studies of other protostars, Fuller et al. (1995) detected H_2 emission in the cavity of

L483. However, the emission was localized to a small section of the cavity, appearing to be an outflow knot within the cavity. Also, Hartmann et al. (1999) did not detect any excess H_2 emission from the IRAS 04325+2402 scattered light nebula. Therefore, the dominant emission mechanism in the NIR to MIR for protostars is scattered continuum emission from the central star and disk and line emission should not significantly contribute to the total flux.

6.8. Predictions

Our dual-cavity model can probably be tested easily by high resolution imaging of the L1527 central object in the MIR. A model image with $0''.11$ pixels convolved with $0''.5$ seeing is shown in Fig. 15. These model images simulate what could be observed from a ground-based MIR telescope at L' , M , or even $7.7\mu\text{m}$. Imaging of this structure is within the capabilities of even modest aperture, infrared optimized telescopes, so long as the PSF is well sampled. As discussed in §3, the central object appears marginally resolved in the IRAC data, but the resolution is too low to observe the small scale structures we are modeling. We would probably see some of the inner envelope structure in the IRAC images if the PSF was more finely sampled at $3.6\mu\text{m}$.

Excellent seeing or adaptive optics (AO) are required to observe the inner envelope structure. But AO observations are difficult for protostars due to the high extinctions obscuring guide stars near the central object. However, at $7.7\mu\text{m}$ the seeing typically can be better than $0''.5$ naturally, thus imaging farther into the MIR may be ideal for observing the inner envelope.

Our model may be an axisymmetric approximation to some complicated feature, thus high resolution observations may not completely reflect the image shown in Fig. 15. We expect high resolution imaging to show some resolved structure that is probably responsible for the complicated morphology observed.

7. Conclusions

We have presented a detailed analysis of infrared scattered light observations of the Class 0 object L1527 (IRAS 04368+2557). L1527 presents itself as a very intriguing object, having bright scattered light emission at NIR to MIR wavelengths, and outflow cavities which are asymmetric in brightness and shape. The extended emission of L1527 is also variable; observations taken a year apart show significant variability. This variability is not constant

for the entire object, the two cavities seem to brighten and fade independently.

We have constructed a model of L1527 which approximates the observed morphology of L1527 in the IRAC and Ks-band images as well as the overall SED. The model uses a modified cavity structure with a narrow cavity near the central protostar and a wider cavity offset from the central protostar. This modified cavity structure creates an apparent central point source in the IRAC images from light scattering on the inner cavity. The inner cavity also casts a shadow on the outer cavity creating the observed separation and dark lane between the outflow cavities. While modeling is inherently not unique at defining the structure of objects, modeling can tell us what the structure is not. This paper shows that L1527 is probably not represented by simple bipolar cavities carved from a TSC envelope, but possibly represented by the structure we have created.

We have demonstrated the importance of simultaneously fitting the morphology of the spatially resolved images as well as the SED. Only fitting the SED could lead to modeling unphysical parameters if the parameter space is not adequately restricted. It can be argued that we also have essentially turned knobs until the imaged looked right. Though, there are clearly asymmetries that are not reflected in our model which impact our SED and image fit. Within the limits of axisymmetry our model fits the observed images and SED quite well. Also, the robustness of our SED fit is probably limited by the uncertain envelope dust model. Our modeled cavity structure may be an axisymmetric approximation of a complex structure resulting from outflow-envelope interactions or binary accretion effects.

The dual-cavity model we have developed is specifically for L1527, however, the model may be more generally applicable. Archived observations from the *Spitzer Space Telescope* of other Class 0 protostars show similar features to L1527; a central object observed between the outflow cavities (Seale & Looney 2008). This central object can probably be resolved using current ground-based MIR instrumentation. This paper demonstrates that observations of the circumstellar envelope by scattered light in conjunction with radiative transfer modeling provide new insights into envelope structure which were previously beyond our reach.

The authors wish to thank B. A. Whitney making her radiative transfer model public and helpful discussions regarding its use and C. Chandler for providing the SCUBA images. We thank the anonymous referee for helpful comments which improved the final paper. We also thank L. W. Looney for his early guidance and Z. Zhu for his assistance in taking the L1527 observations with TIFKAM. We are grateful to the staff of MDM Observatory for their support during TIFKAM observations. TIFKAM was funded by The Ohio State University, the MDM consortium, MIT, and NSF grant AST-9605012. The HAWAII2 array used in TIFKAM was purchased with an NSF Grant to Dartmouth University. This

publication makes use of data products from the Two Micron All Sky Survey, which is a joint project of the University of Massachusetts and the Infrared Processing and Analysis Center/California Institute of Technology, funded by the National Aeronautics and Space Administration and the National Science Foundation. J.T., L.H., and N.C. acknowledge support from the University of Michigan.

REFERENCES

- Adams, F. C., Lada, C. J., & Shu, F. H. 1987, *ApJ*, 312, 788
- Andre, P., Ward-Thompson, D., & Barsony, M. 1993, *ApJ*, 406, 122
- Andrews, S. M., & Williams, J. P. 2007, *ApJ*, 659, 705
- Arce, H. G., & Sargent, A. I. 2006, *ApJ*, 646, 1070
- Bate, M. R., & Bonnell, I. A. 1997, *MNRAS*, 285, 33
- Beichman, C. A., Neugebauer, G., Habing, H. J., Clegg, P. E., & Chester, T. J., eds. 1988, *Infrared astronomical satellite (IRAS) catalogs and atlases. Volume 1: Explanatory supplement, Vol. 1*
- Benson, P. J., & Myers, P. C. 1989, *ApJS*, 71, 89
- Bergin, E. A., & Tafalla, M. 2007, *ArXiv e-prints*, 705
- Bontemps, S., Andre, P., Terebey, S., & Cabrit, S. 1996, *A&A*, 311, 858
- Calvet, N., & Gullbring, E. 1998, *ApJ*, 509, 802
- Calvet, N., Hartmann, L., Kenyon, S. J., & Whitney, B. A. 1994, *ApJ*, 434, 330
- Chandler, C. J., & Richer, J. S. 2000, *ApJ*, 530, 851
- Chen, H., Myers, P. C., Ladd, E. F., & Wood, D. O. S. 1995, *ApJ*, 445, 377
- Cunningham, A., Frank, A., & Hartmann, L. 2005, *ApJ*, 631, 1010
- D’Alessio, P., Calvet, N., & Hartmann, L. 2001, *ApJ*, 553, 321
- D’Alessio, P., Calvet, N., Hartmann, L., Franco-Hernández, R., & Servín, H. 2006, *ApJ*, 638, 314
- Delamarter, G., Frank, A., & Hartmann, L. 2000, *ApJ*, 530, 923

- Draine, B. T., & Lee, H. M. 1984, *ApJ*, 285, 89
- Dullemond, C. P., Dominik, C., & Natta, A. 2001, *ApJ*, 560, 957
- Eiroa, C., Miranda, L. F., Anglada, G., Estalella, R., & Torrelles, J. M. 1994, *A&A*, 283, 973
- Fazio, G. G., et al. 2004, *ApJS*, 154, 10
- Flaherty et al. 2007, *ApJ*, 663, 1069
- Fuller, G. A., Lada, E. A., Masson, C. R., & Myers, P. C. 1995, *ApJ*, 453, 754
- Furlan, E., et al. 2007, *ApJ* in press.
- Gueth, F., Guilloteau, S., & Bachiller, R. 1996, *A&A*, 307, 891
- Hartmann, L. 1998, *Accretion Processes in Star Formation* (Accretion processes in star formation / Lee Hartmann. Cambridge, UK ; New York : Cambridge University Press, 1998. (Cambridge astrophysics series ; 32) ISBN 0521435072.)
- Hartmann, L., Calvet, N., & Boss, A. 1996, *ApJ*, 464, 387
- Hartmann, L., Calvet, N., Allen, L., Chen, H., & Jayawardhana, R. 1999, *AJ*, 118, 1784
- Hartmann, L., et al. 2005, *ApJ*, 629, 881
- Hogerheijde, M. R., van Dishoeck, E. F., Blake, G. A., & van Langevelde, H. J. 1998, *ApJ*, 502, 315
- Houck, J. R., et al. 2004, *ApJS*, 154, 18
- Hunt, L. K., Mannucci, F., Testi, L., Migliorini, S., Stanga, R. M., Baffa, C., Lisi, F., & Vanzi, L. 1998, *AJ*, 115, 2594
- Indebetouw, R., et al. 2005, *ApJ*, 619, 931
- Kenyon, S. J., Brown, D. I., Tout, C. A., & Berlind, P. 1998, *AJ*, 115, 2491
- Kenyon, S. J., Calvet, N., & Hartmann, L. 1993, *ApJ*, 414, 676
- Kim, S.-H., Martin, P. G., & Hendry, P. D. 1994, *ApJ*, 422, 164
- Lada, C. J. 1987, *Star Forming Regions*, 115, 1
- Ladd, E. F., et al. 1991, *ApJ*, 382, 555

- Li, A., & Draine, B. T. 2001, *ApJ*, 554, 778
- Loinard, L., Rodríguez, L. F., D’Alessio, P., Wilner, D. J., & Ho, P. T. P. 2002, *ApJ*, 581, L109
- Looney, L. W., Tobin, J. J., & Kwon, W. 2007, *ApJ*, 670, L131
- Meakin, C. A., Bieging, J. H., Latter, W. B., Hora, J. L., & Tielens, A. G. G. M. 2003, *ApJ*, 585, 482
- Motte, F., & André, P. 2001, *A&A*, 365, 440
- Muzerolle, J., Calvet, N., Hartmann, L., & D’Alessio, P. 2003, *ApJ*, 597, L149
- Noriega-Crespo, A., et al. 2004, *ApJS*, 154, 352
- Ohashi, N., Hayashi, M., Ho, P. T. P., & Momose, M. 1997, *ApJ*, 475, 211
- Osorio, M., D’Alessio, P., Muzerolle, J., Calvet, N., & Hartmann, L. 2003, *ApJ*, 586, 1148
- Padgett, D., et al. 2006, in *Bulletin of the American Astronomical Society*, Vol. 38, *Bulletin of the American Astronomical Society*, 947–+
- Padgett, D. L., Brandner, W., Stapelfeldt, K. R., Strom, S. E., Terebey, S., & Koerner, D. 1999, *AJ*, 117, 1490
- Pogge, R. W., et al. 1998, *Proc. SPIE*, 3354, 414
- Pollack, J. B., Hollenbach, D., Beckwith, S., Simonelli, D. P., Roush, T., & Fong, W. 1994, *ApJ*, 421, 615
- Ragan, S. E., Bergin, E. A., Plume, R., Gibson, D. L., Wilner, D. J., O’Brien, S., & Hails, E. 2006, *ApJS*, 166, 567
- Rieke, G. H., et al. 2004, *ApJS*, 154, 25
- Robitaille, T. P., Whitney, B. A., Indebetouw, R., & Wood, K. 2007, *ApJS*, 169, 328
- Robitaille, T. P., Whitney, B. A., Indebetouw, R., Wood, K., & Denzmore, P. 2006, *ApJS*, 167, 256
- Román-Zúñiga, C., Lada, C., Muench, A., & Alves, J. 2007, *ArXiv e-prints*, 704
- Seale, J. P., & Looney, L. W. 2008, *ApJ* submitted

- Shirley, Y. L., Evans, II, N. J., Rawlings, J. M. C., & Gregersen, E. M. 2000, *ApJS*, 131, 249
- Shu, F. H., Adams, F. C., & Lizano, S. 1987, *ARA&A*, 25, 23
- Simon, R., Jackson, J. M., Rathborne, J. M., & Chambers, E. T. 2006, *ApJ*, 639, 227
- Skrutskie, M. F., et al. 2006, *AJ*, 131, 1163
- Stark, D. P., Whitney, B. A., Stassun, K., & Wood, K. 2006, *ApJ*, 649, 900
- Swift, J. J., & Welch, W. J. 2008, *ApJS*, 174, 202
- Tannirkulam, A., Harries, T. J., & Monnier, J. D. 2007, *ApJ*, 661, 374
- Terebey, S., Shu, F. H., & Cassen, P. 1984, *ApJ*, 286, 529
- Tobin, J. J., Looney, L. W., Mundy, L. G., Kwon, W., & Hamidouche, M. 2007, *ApJ*, 659, 1404
- Tuthill, P. G., Monnier, J. D., & Danchi, W. C. 2001, *Nature*, 409, 1012
- Watson, A. M., & Stapelfeldt, K. R. 2007, *AJ*, 133, 845
- Whitney, B. A., & Hartmann, L. 1993, *ApJ*, 402, 605
- Whitney, B. A., Wood, K., Bjorkman, J. E., & Wolff, M. J. 2003b, *ApJ*, 591, 1049
- Whitney, B. A., Wood, K., Bjorkman, J. E., & Cohen, M. 2003a, *ApJ*, 598, 1079
- Whittet, D. C. B., Gerakines, P. A., Hough, J. H., & Shenoy, S. S. 2001, *ApJ*, 547, 872
- Wood et al. 2001, *ApJ*, 561, 299
- Ybarra et al. 2006, *ApJ*, 647, L159
- Zhou, S., Evans, II, N. J., & Wang, Y. 1996, *ApJ*, 466, 296

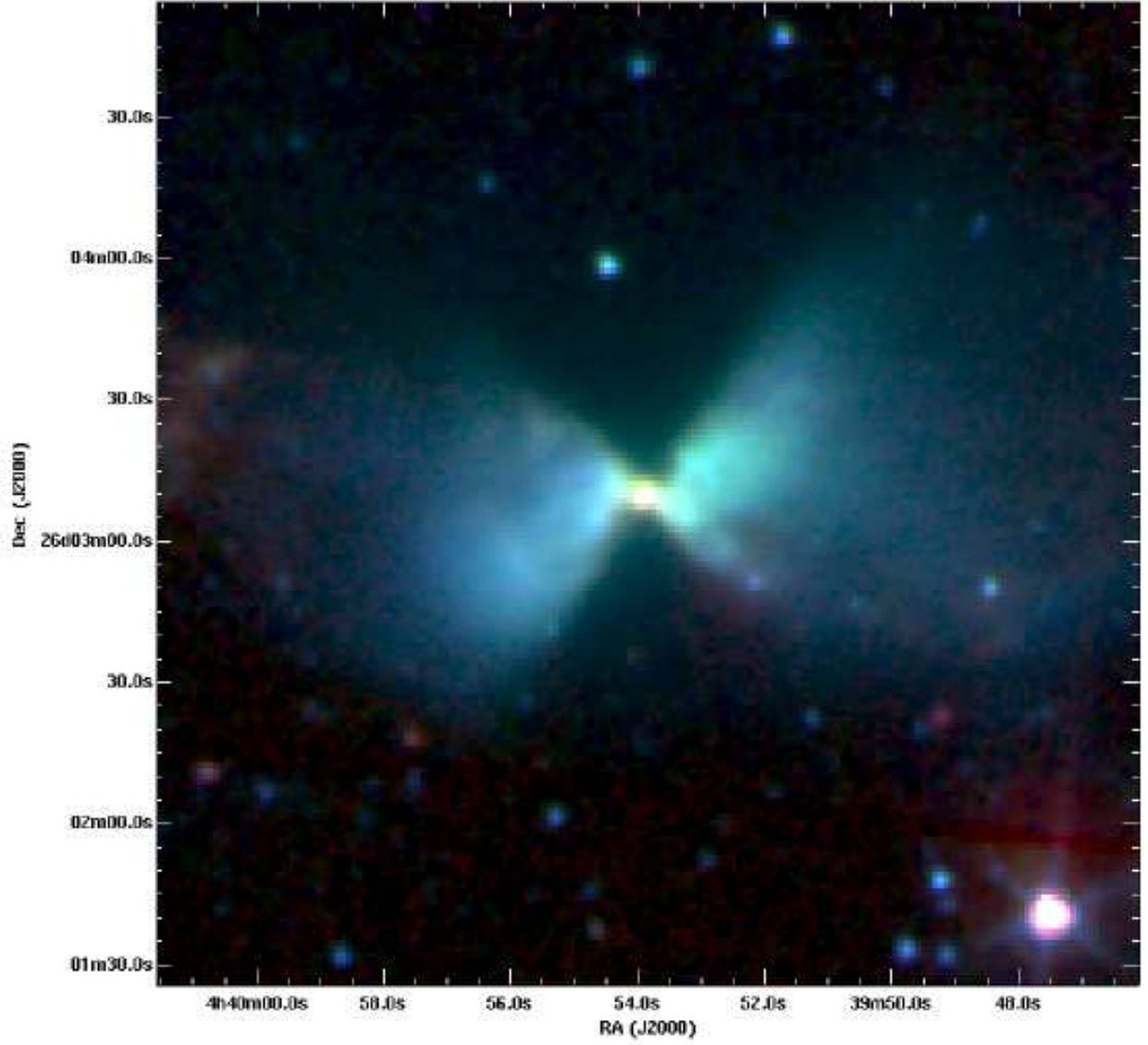


Fig. 1.— False-color IRAC image of L1527 IRS (IRAS 04368+2557), Blue: $3.6\mu\text{m}$, Green: $4.5\mu\text{m}$, and Red: $8.0\mu\text{m}$. Image box is $200''$ on a side, corresponding to ~ 28000 AU at a distance of 140pc.

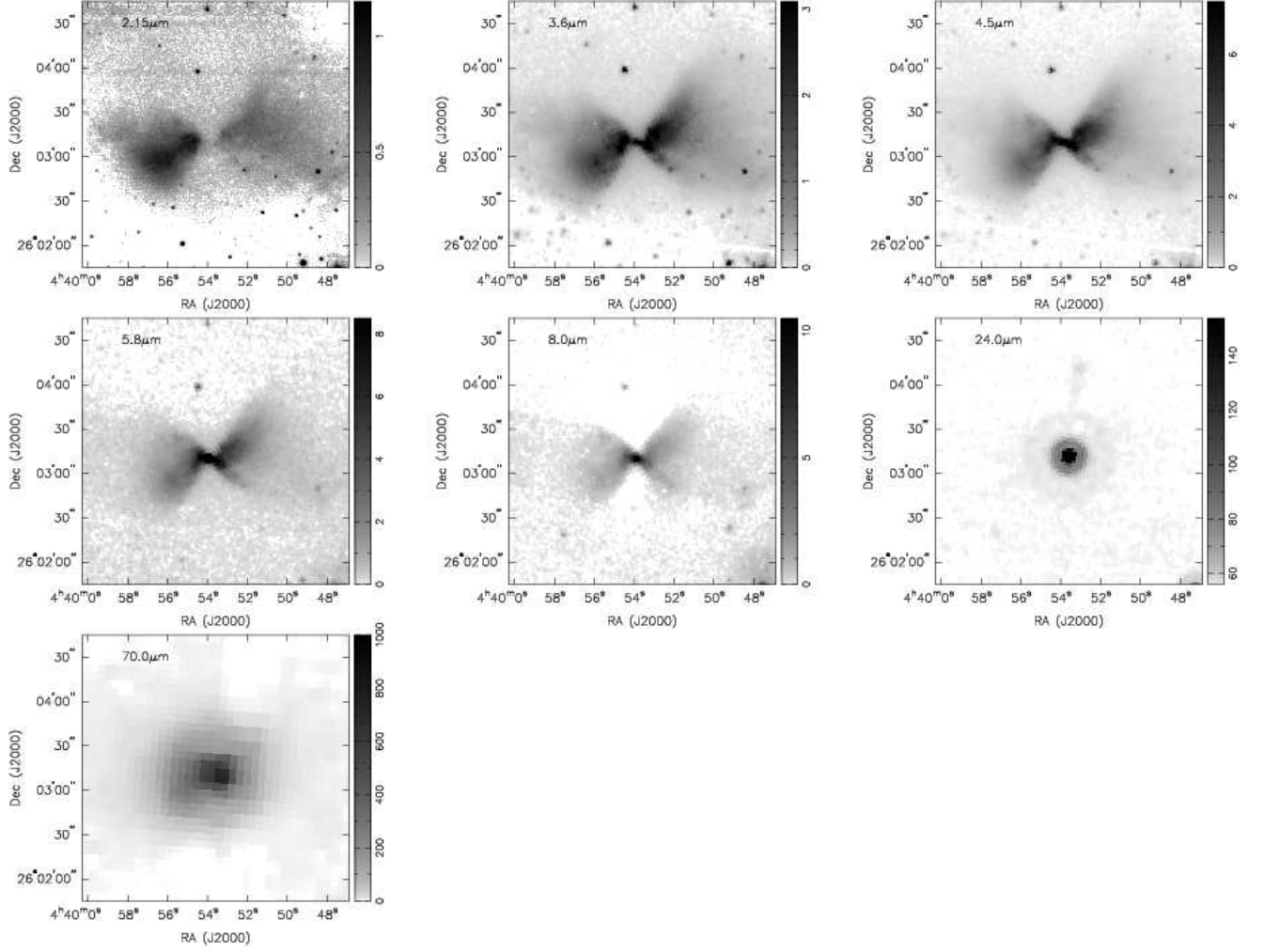


Fig. 2.— Near-infrared and *Spitzer* images of L1527 as observed by TIFKAM, IRAC, and MIPS. Images are 180'' on a side, corresponding to ~ 25000 AU at a distance of 140pc. Units of intensity are MJy/sr.

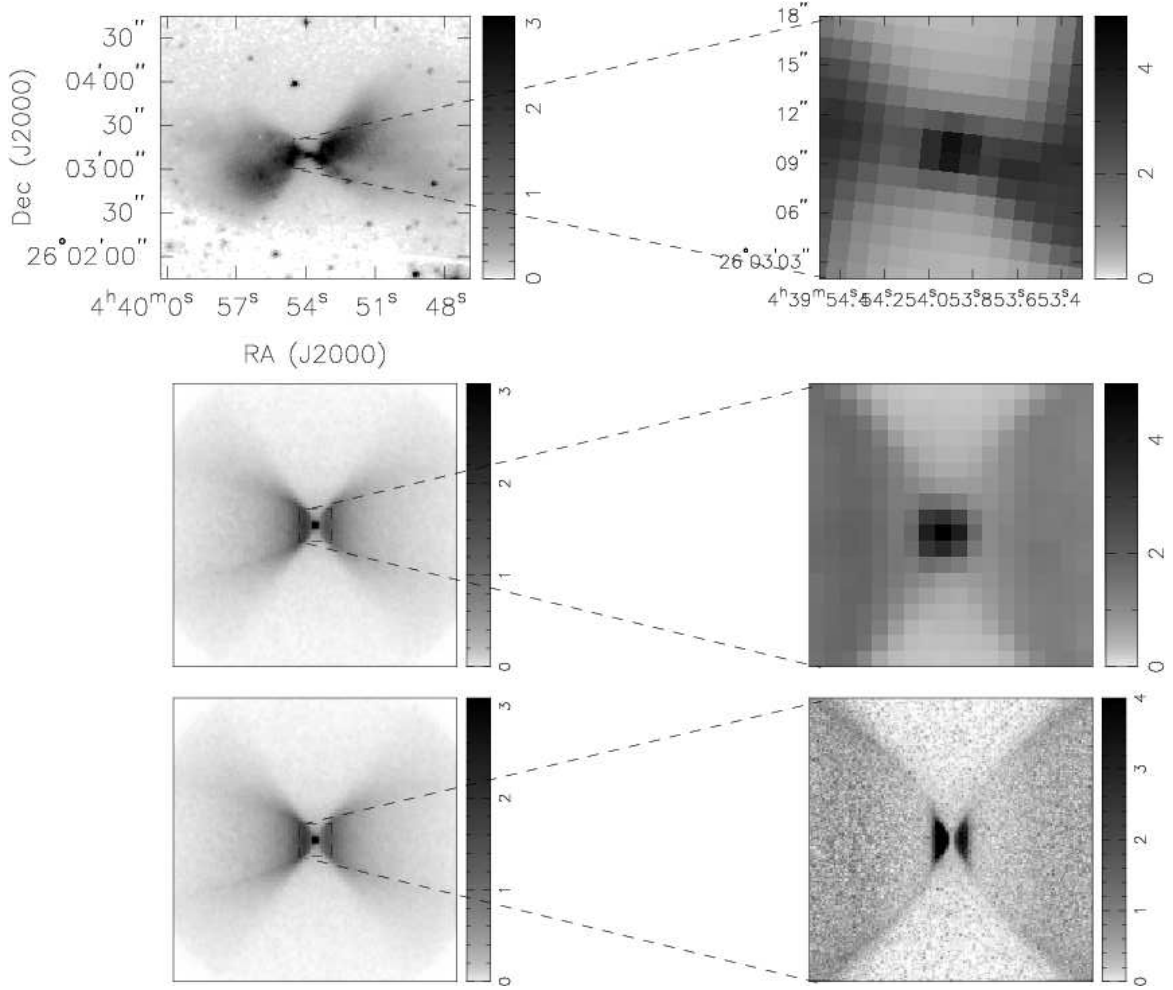


Fig. 3.— Top: IRAC 3.6 μ m image of L1527 zooming on on the ‘neck’ as described in §3. Middle: Best fitting model image zooming in on inner envelope structure. Bottom: Best fitting model image with unconvolved view of of the inner envelope. Units are MJy/sr.

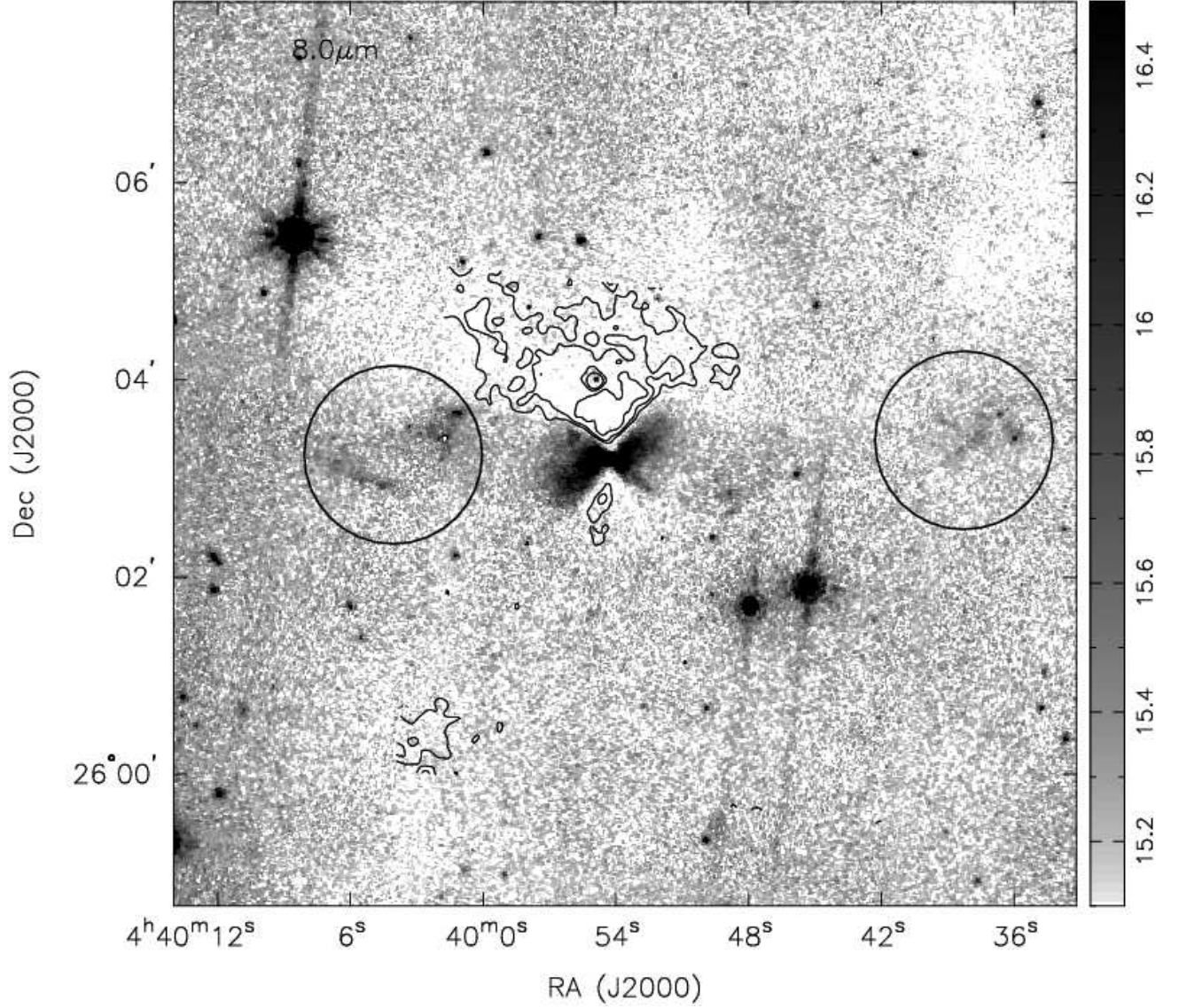


Fig. 4.— Wide-field view of L1527 region at 8.0μm. Herbig-Haro objects in apparent association with L1527 are circled. These objects infer an outflow PA $\sim 90^\circ$. Assuming an outflow velocity of 100km/s, these outflow knots have a dynamical age of only 1100 - 1600 yrs. Contours are 8.0μm optical depth contours corresponding to $\tau = 0.08, 0.10, 0.126$ and 0.16. The contours match up with the regions where there is a lack of background emission. Units are MJy/sr.

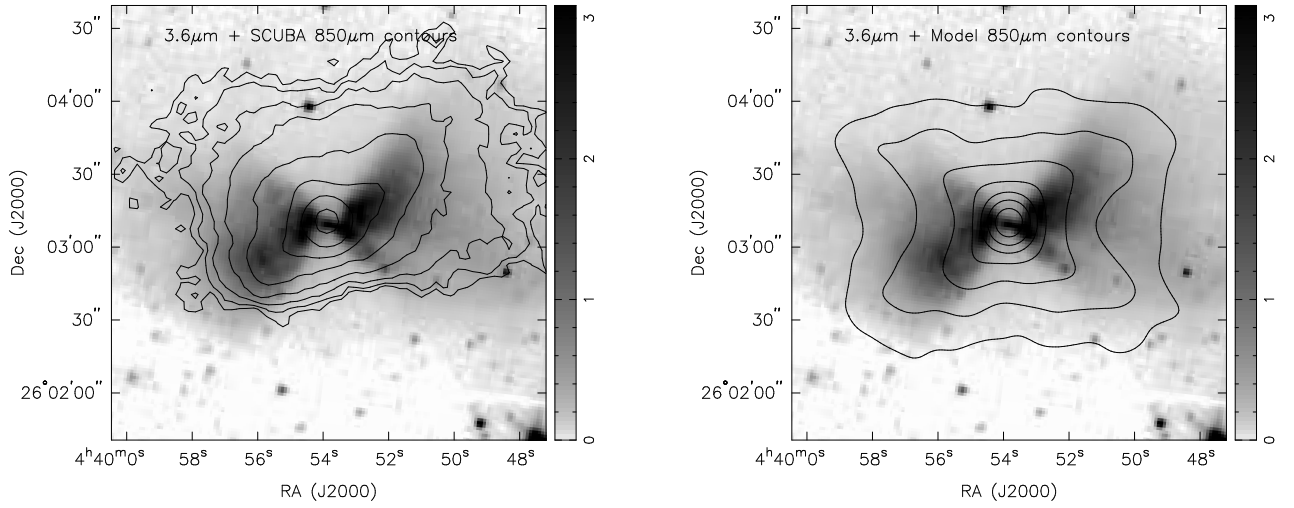


Fig. 5.— Left: IRAC $3.6\mu\text{m}$ image with $850\mu\text{m}$ SCUBA contours from Chandler & Richer (2000). Right: IRAC $3.6\mu\text{m}$ image with model $850\mu\text{m}$ contours. Notice the boxiness of the contours and how the south side flux falls off rapidly as compared to the north side flux in the SCUBA image. The model image is able to duplicate the boxy features of the SCUBA data on the inner contours. The SCUBA contours clearly show an asymmetry corresponding to the bright patches as observed in the IRAC images. The contours are 2.07, 3.49, 5.58, 9.91, 16.71, 28.16, 47.46, and 80.0 MJy/sr.

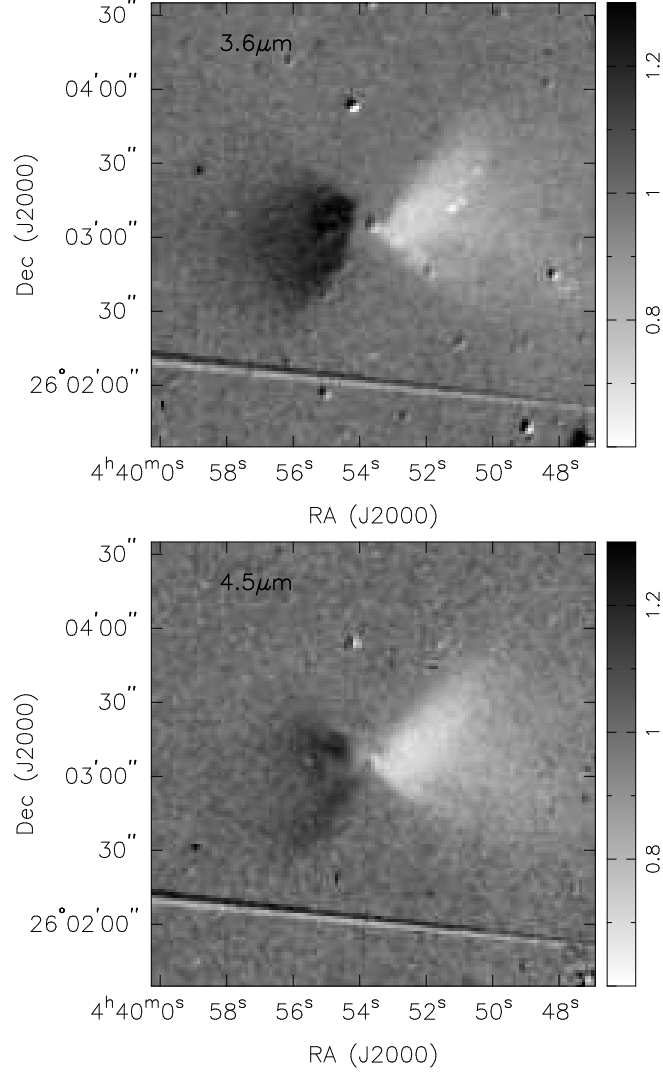


Fig. 6.— 2004 epoch IRAC images divided by the 2005 epoch IRAC images. The lighter gray to white signifies less flux in the 2004 epoch, while darker gray means more flux. The variability is present in IRAC Channels 3 and 4, but the noise is much higher.

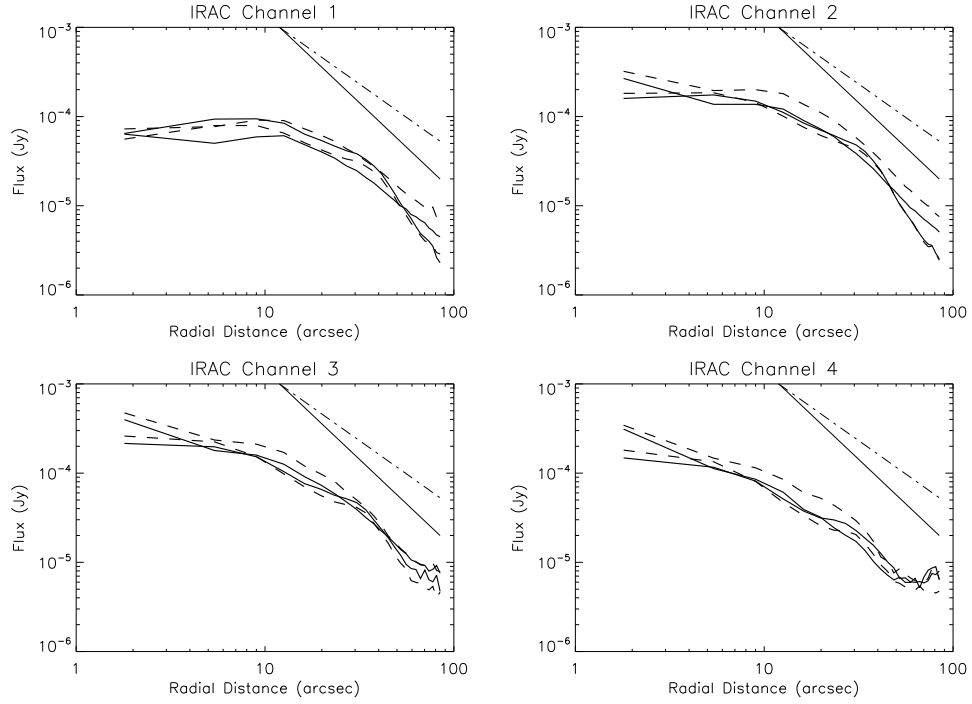


Fig. 7.— Average flux in a $3''.6$ width annulus measured radially from the center. The 2004 (solid lines) and 2005 (dashed lines) epochs are plotted, there are two lines per epoch corresponding to the east and west cavities. The straight lines drawn in the upper right correspond to power-laws of -2 (solid line) and -1.5 (dot-dashed line).

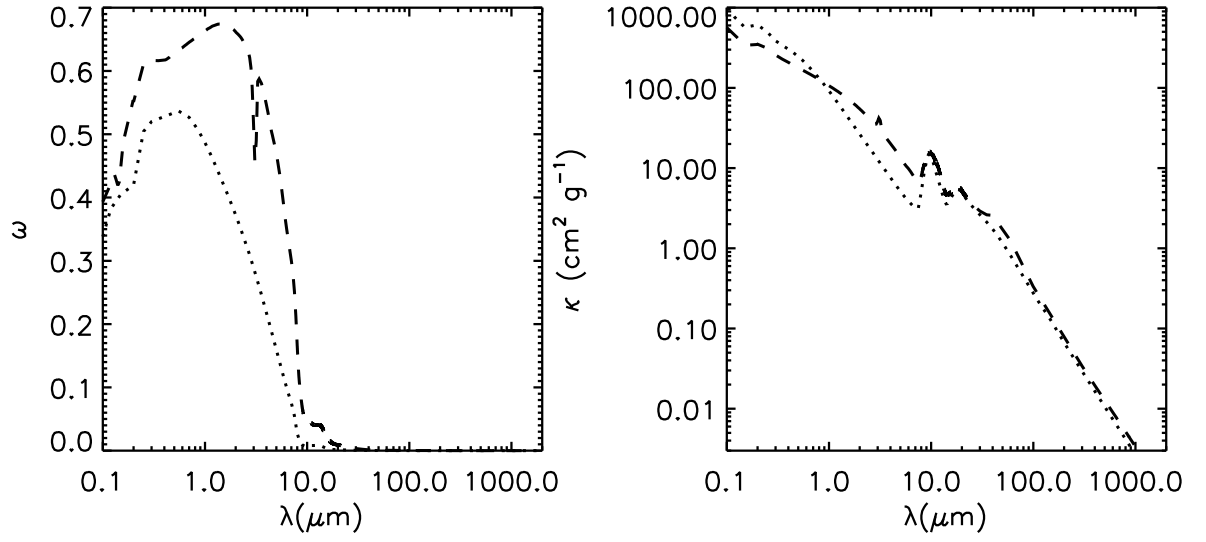


Fig. 8.— Albedo (left) and opacity (right) curves of dust models. The dashed line is the larger grain dust model we used, and the dotted line is an ISM dust model (Kim et al. 1994).

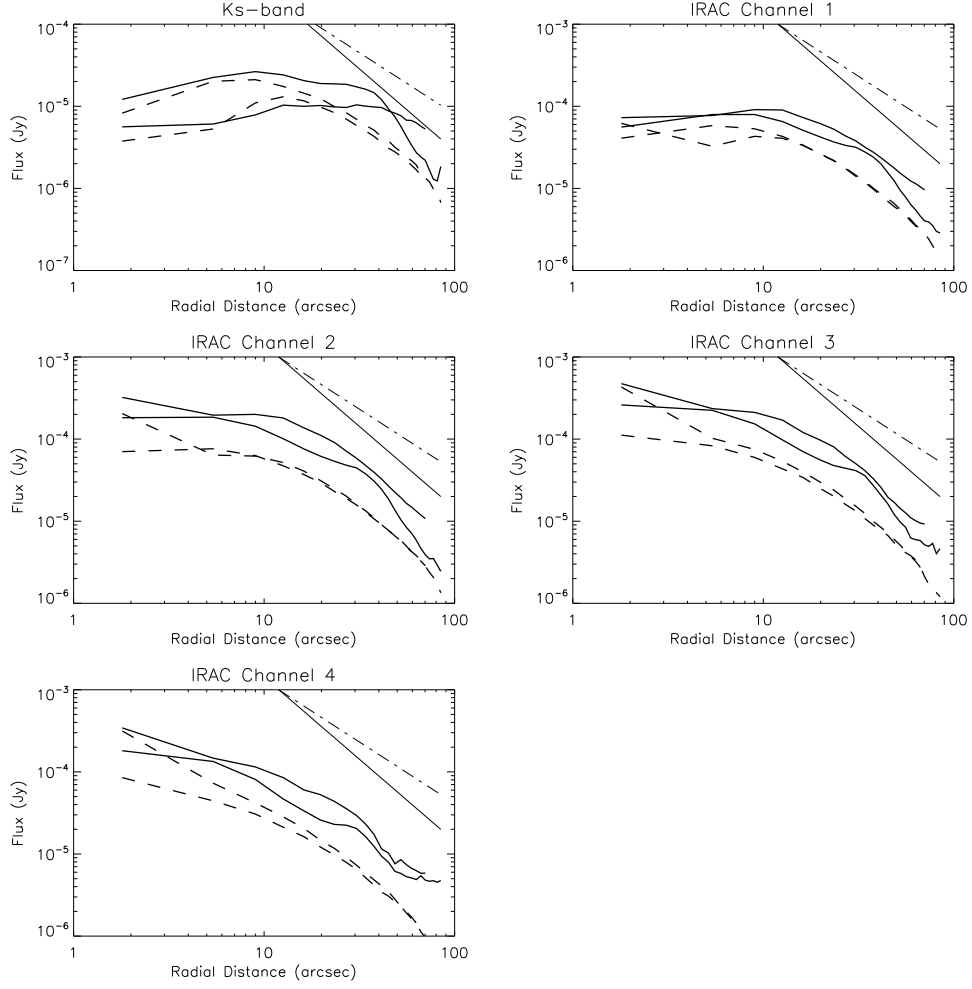


Fig. 9.— Same as Fig. 7 except the data (solid lines) and model (dashed lines) are plotted. The data the average of the two epochs, except Ks-band.

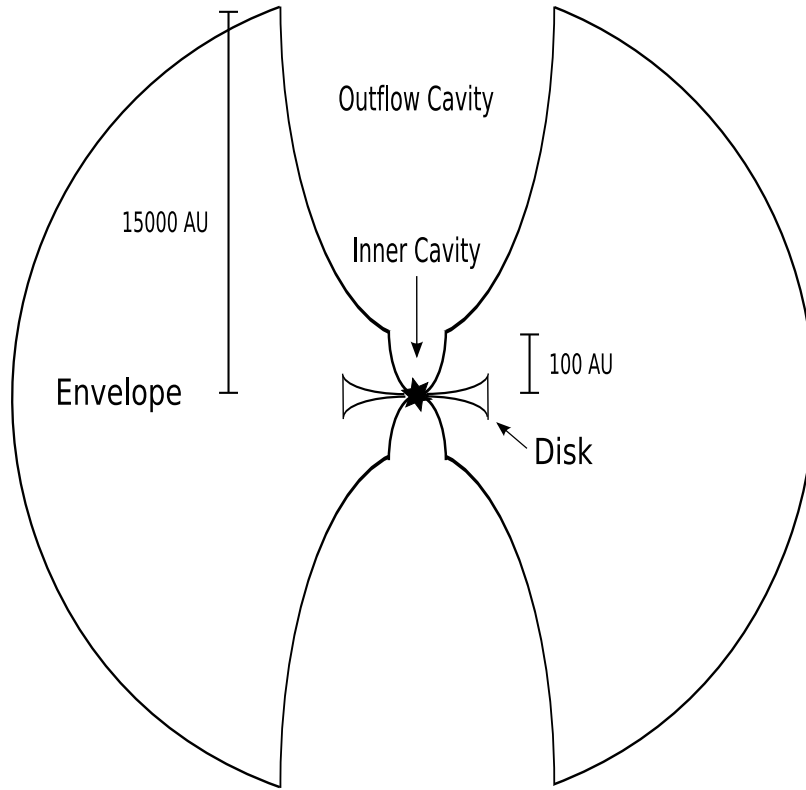


Fig. 10.— Schematic representation of modeled cavity and envelope structure. Inner envelope regions are not drawn to scale.

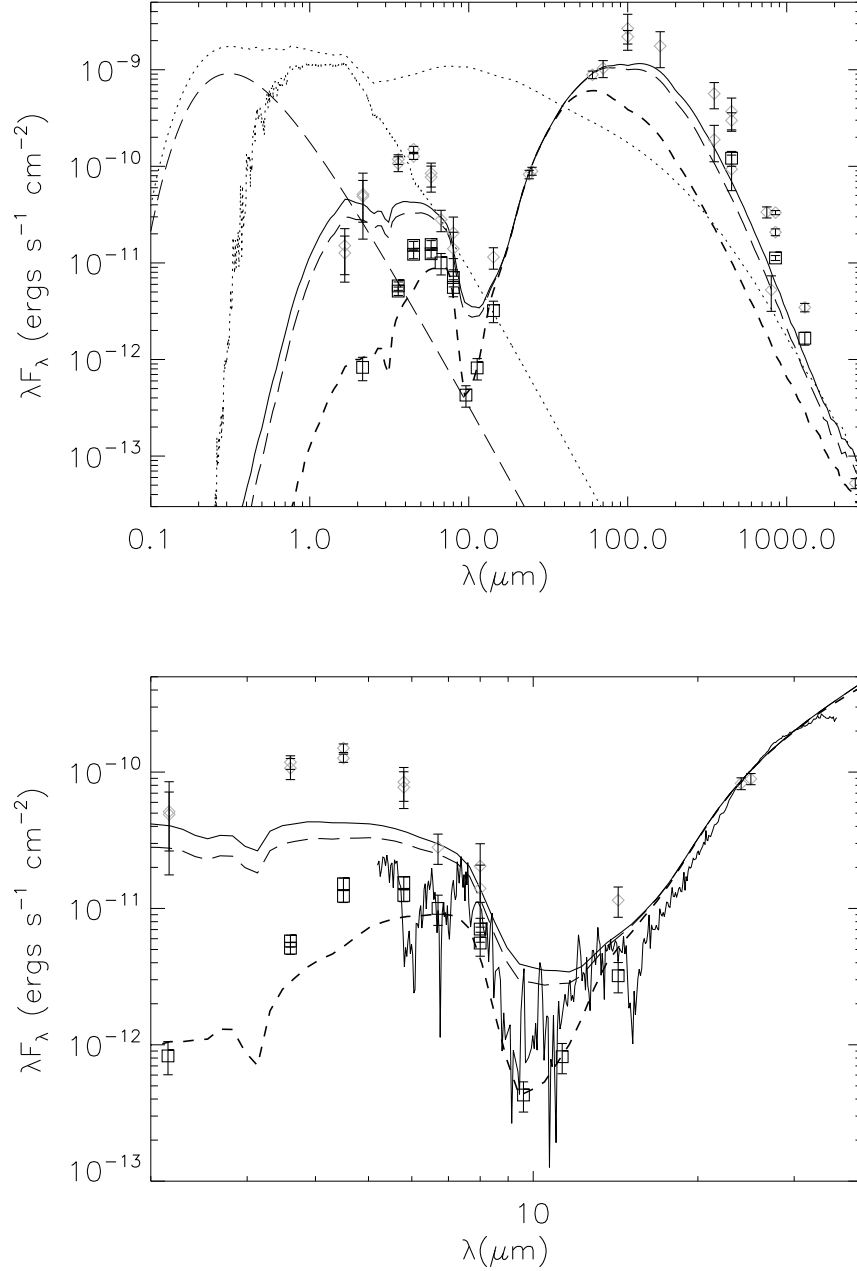


Fig. 11.— The full SED of L1527 (Top) with the model, excluding the IRS spectrum. A zoomed in portion of the SED (Bottom) is plotted with IRS spectrum from 2 - 40 μ m. The model SED is plotted for apertures of 10000 AU (solid line), 6000 AU (long-dashed line), and 1000 AU (short-dashed line). Photometry taken with apertures of 71''4 (diamonds) and 7''14 (boxes) corresponding to 10000 AU and 1000 AU apertures are plotted. The long wavelength data have varying apertures which are comparable to the 6000 and 10000 AU apertures. We also plot the spectrum of the central protostar and disk (coarse dotted line) illuminating the envelope viewed face-on; the 4000K stellar atmosphere (fine dotted line) and the accretion shock (long dashed line at short λ) of the infalling material onto the star.

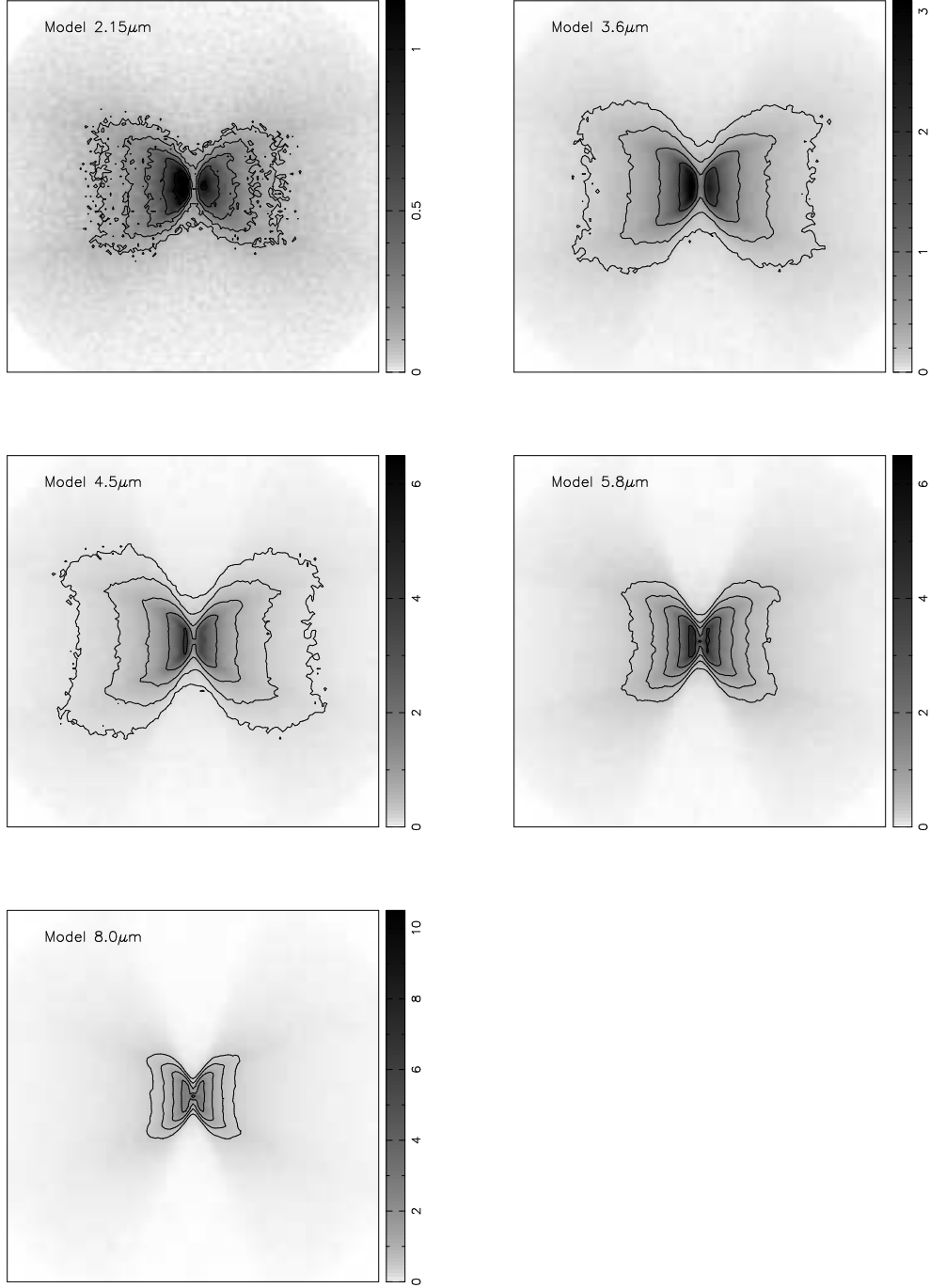


Fig. 12.— Model images generated using a single cavity; all other parameters are identical to the dual-cavity model. In comparison to the observations, these images clearly do a much worse job reproducing the data than the dual-cavity images. Notice the lack of a central source and thick dark lane in contrast to the dual-cavity model. Images are 180'' on a side, corresponding to ~ 25000 AU at a distance of 140pc, units are MJy/sr.

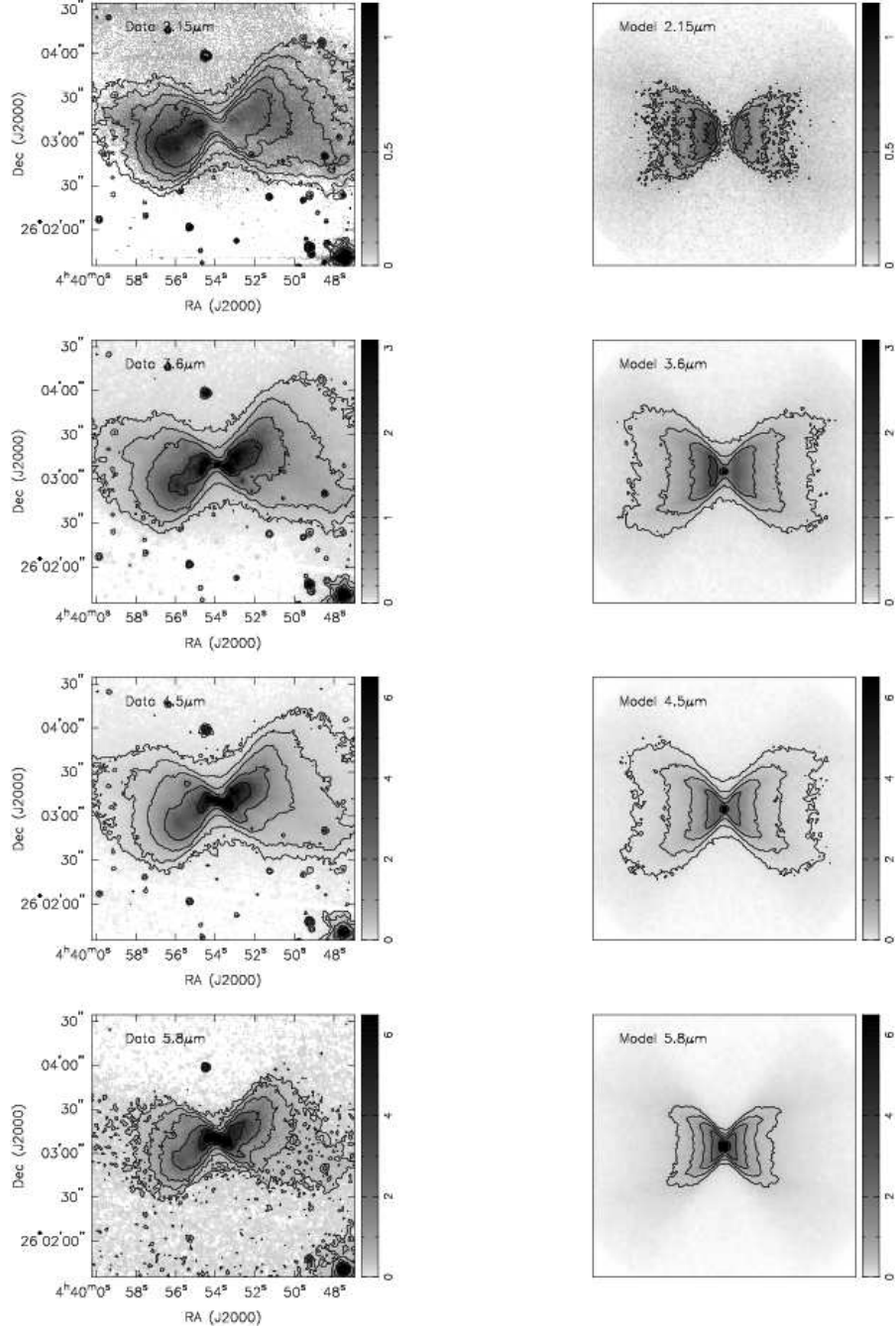


Fig. 13a.— Left: L1527 images as in Fig. 2, Right: Best fit model. (a) Images for 2.15, 3.6, 4.5, and $5.8\mu\text{m}$, (b) Images for 8.0, 24, and $70\mu\text{m}$. The contours for the L1527 data on the left clearly show the azimuthal asymmetry. Images are $180''$ on a side, corresponding to ~ 25000 AU at a distance of 140pc, units are MJy/sr.

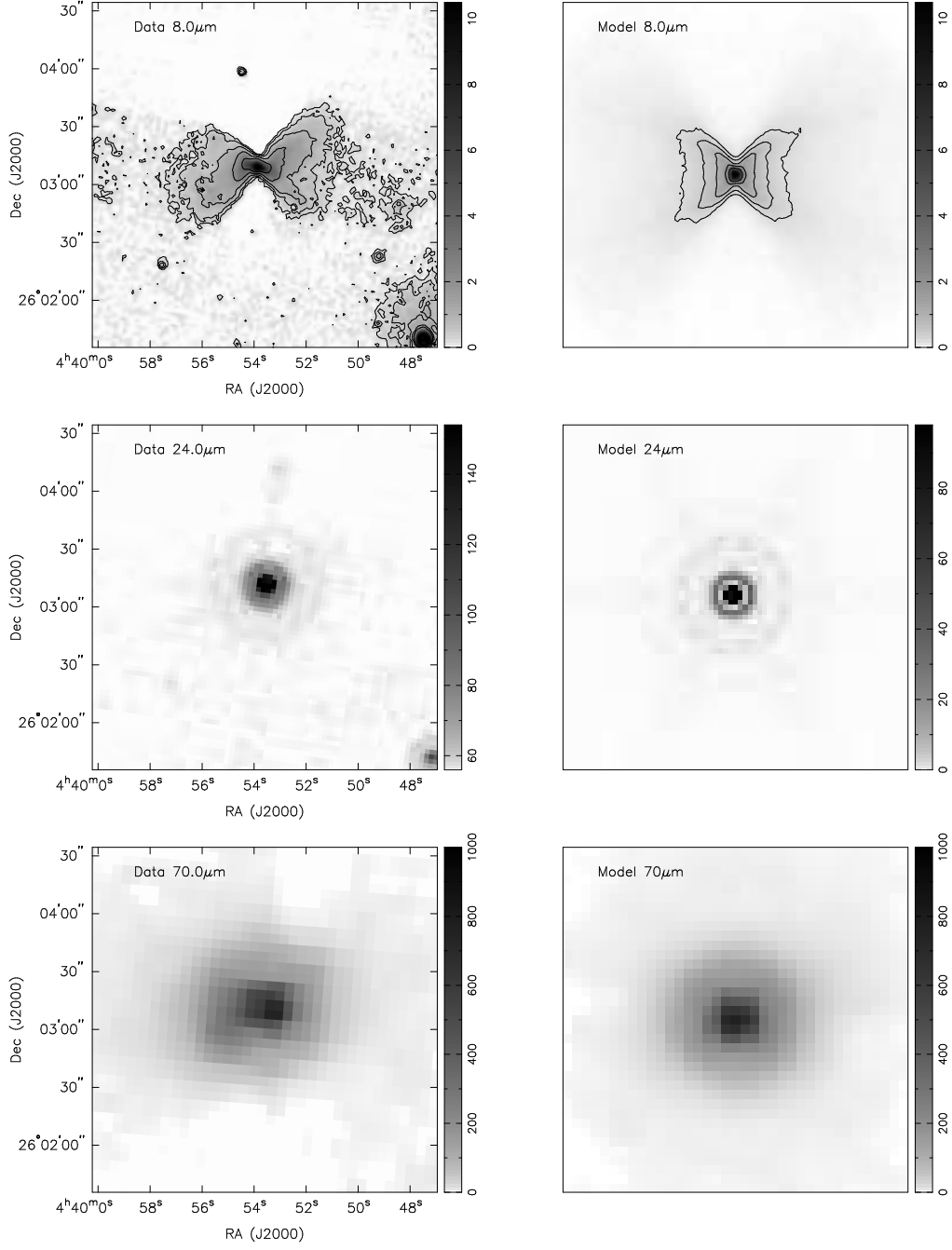


Fig. 13b.—

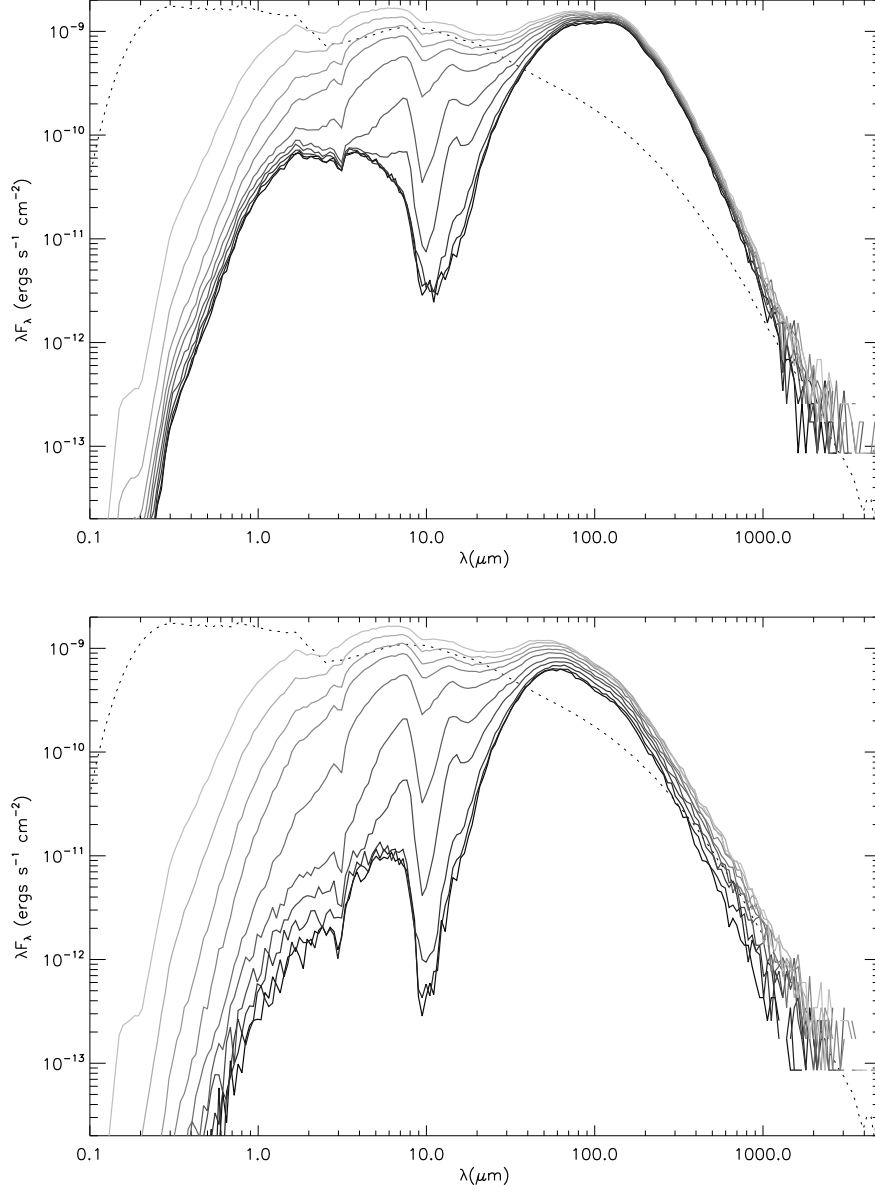


Fig. 14.— SEDs of the best fitting model from L1527 at multiple inclinations. The lines plotted from lightest to darkest correspond to inclinations of 18, 32, 31, 49, 57, 63, 70, 76, 81, and 87° measured in apertures of 5000 AU (left panel) and 1000 AU (right panel). The dotted line is the central star and disk as viewed face-on.

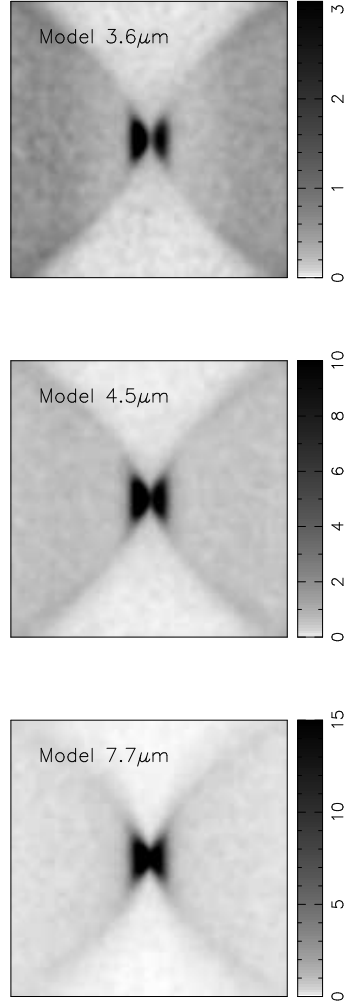


Fig. 15.— Simulated images convolved with 0".5 seeing. These images are comparable to the abilities of current ground-based infrared telescopes. The 3.6 μ m image is comparable to L'-band, 4.5 μ m is comparable to M'-band, and the 7.7 μ m is comparable to a narrow-band filter.

Table 1. Photometry

Wavelength (μm)	F_λ (mJy)	Aperture (arcsec)	Aperture ^a Correction	Instrument	Observation Date	References
1.66	7.0 ± 3.5	71.43	-	TIFKAM	12-27-2007	1
1.66	8.35 ± 4.17	71.43	-	2MASS	10-14-1998	1
2.16	0.594 ± 0.162	71.43	-	TIFKAM	12-27-2007	1
2.16	35.2 ± 16.2	71.43	-	TIFKAM	12-27-2007	1
2.16	36.94 ± 24.3	71.43	-	2MASS	10-14-1998	1
3.6	6.936 ± 0.69	71.43	1.014	IRAC	03-07-2004	1
" "	141.8 ± 16.2	71.43	0.9164	IRAC	03-07-2004	1
3.6	6.132 ± 0.61	71.43	1.014	IRAC	02-23-2005	1
" "	128.3 ± 22.6	71.43	0.9164	IRAC	02-23-2005	1
4.5	22.75 ± 2.28	71.43	1.061	IRAC	03-07-2004	1
" "	225.1 ± 16.3	71.43	0.9463	IRAC	03-07-2004	1
4.5	18.43 ± 1.84	71.43	1.061	IRAC	02-23-2005	1
" "	190.0 ± 13.1	71.43	0.9463	IRAC	02-23-2005	1
5.8	29.93 ± 2.99	71.43	0.9918	IRAC	03-07-2004	1
" "	149.5 ± 45.0	71.43	0.7926	IRAC	03-07-2004	1
5.8	24.08 ± 2.41	71.43	0.9918	IRAC	02-23-2005	1
" "	163.4 ± 45.5	71.43	0.7926	IRAC	02-23-2005	1
6.7	22.36 ± 5.6	7.2	-	ISOCAM	10-02-1997	1
" "	62.68 ± 15.7	36	-	ISOCAM	10-02-1997	1
8.0	18.83 ± 3.8	71.43	0.9423	IRAC	03-07-2004	1
" "	54.54 ± 25.0	71.43	0.7629	IRAC	03-07-2004	1
8.0	14.87 ± 3.0	71.43	0.9423	IRAC	02-23-2005	1
" "	37.43 ± 18.0	71.43	0.7629	IRAC	02-23-2005	1
9.6	1.37 ± 0.34	7.2	-	ISOCAM	10-02-1997	1
11.3	3.081 ± 0.77	7.2	-	ISOCAM	10-02-1997	1
14.3	15.3 ± 3.8	7.2	-	ISOCAM	10-02-1997	1
" "	54.76 ± 13.7	36	-	ISOCAM	10-02-1997	1
24	660.6 ± 66	13	1.167	MIPS	03-05-2005	1
25	743.6 ± 70	45 x 300	-	IRAS	-	2
60	17770 ± 1600	90 x 300	-	IRAS	-	2
70	24170 ± 4834	75	1.0	MIPS	03-05-2005	1

Table 1—Continued

Wavelength (μm)	F_λ (mJy)	Aperture (arcsec)	Aperture ^a Correction	Instrument	Observation Date	References
100	73260 ± 11700	180 x 300	-	IRAS	-	2
100	89000 ± 36000	60	-	Yerkes (KAO) ^b	03-1987	3
160	94000 ± 38000	60	-	Yerkes (KAO)	03-1987	3
350	22000 ± 9000	60	-	Yerkes (IRTF)	10-1987	3
350	66000 ± 20000	45	-	SCUBA	01-1998	4
450	14000 ± 5600	60	-	JCMT/UKT	01-1989	4
450	44800 ± 9000	45	-	SCUBA	01-1998	4
450	18200 ± 3200	40	-	SCUBA	01-1998	5
450	55500 ± 20900	120	-	SCUBA	01-1998	5
750	8400 ± 1100	45	-	SCUBA	01-1998	4
800	1400 ± 560	60	-	JCMT/UKT	01-1989	3
850	5900 ± 480	45	-	SCUBA	01-1998	4
850	3190 ± 190	40	-	SCUBA	01-1998	5
850	9410 ± 460	120	-	SCUBA	01-1998	5
1300	720 ± 110	40	-	SCUBA	01-1998	5
1300	1500	30	-	IRAM	-	6
2700	47 ± 5.6	60 x 60	-	NMA ^c	01-1995	7

^aCorrections for IRAC data were derived from the prescription for extended source calibration on the *Spitzer Science Center* website. Corrections for MIPS data are taken from the MIPS data handbook.

^bKuiper Airborne Observatory

^cNobeyama Millimeter Array

References. — (1) This work; (2) Beichman et al. (1988); (3) Ladd et al. (1991); (4) Chandler & Richer (2000); (5) Shirley et al. (2000); (6) Motte & André (2001); (7) Ohashi et al. (1997)

Table 2. Model parameters

Parameter	Description	This paper	KCH93	R07 Standard Integrated	R07 Full SED Resolved	R07 IRAC SED Resolved	Furlan 2007
$R_*(R_\odot)$	Stellar radius	2.09	-	-	8.21	21.57	2.0
$T_*(K)$	Stellar temperature	4000	-	2932 - 3869	4260	4360	4000
$L_*(L_\odot)$	System luminosity	2.75	1.35	0.64 - 3.84	20	155	1.8
$M_*(M_\odot)$	Stellar mass	0.5	-	0.15 - 0.59	1.46	4.07	-
$M_{disk}(M_\odot)$	Disk mass	0.1	-	6.3×10^{-5} - 0.016	8.58×10^{-4}	0.142	-
$h(100)$ (AU)	Disk scale height at 100AU	10.52	-	3.18 - 9.67	8.09	3.891	10
α	Disk radial density exponent	2.125	-	-	2.155	2.042	-
β	Disk scale height exponent	1.125	-	-	1.155	1.042	-
$\dot{M}_{disk}(M_\odot \text{ yr}^{-1})$	Disk accretion rate	3.0×10^{-7}	-	9.77×10^{-12} - 5.01×10^{-8}	1.98×10^{-8}	7.29×10^{-7}	-
$R_{trunc}(R_*)$	Magnetosphere co-rotation radius	3.0	-	-	5.0	5.0	-
F_{spot}	Fractional area of accretion hotspot	0.01	-	0.01	0.01	0.01	-
$R_{disk,min}(R_*)$	Disk inner radius	14.25	-	R_{dd}	7.84	8.33	1.0
$R_{disk,max}(AU)$	Disk outer radius	75	-	33.8 - 1303.3	58.398	33.703	200
$R_c(AU)$	Centrifugal radius	75	300	-	58.398	33.703	200
$R_{env,min}(R_*)$	Envelope inner radius	42.75	-	-	7.84	8.33	-
$R_{env,max}(AU)$	Envelope outer radius	15000	3000	-	16200	9120	10000
$\dot{M}_{env}(M_\odot \text{ yr}^{-1})$	Envelope mass infall rate	1.00×10^{-5}	4.22×10^{-5a}	$0.911 - 5.05 \times 10^{-5}$	1.37×10^{-4}	2.63×10^{-4}	5.34×10^{-6a}
$\rho_1(g \text{ cm}^{-3})$	Envelope Density at 1 AU	3.75×10^{-14}	3.16×10^{-13}	$0.341 - 1.89 \times 10^{-13a}$	8.77×10^{-13}	2.81×10^{-12}	1.00×10^{-14}
b_{in}	Inner cavity shape exponent	1.5	-	-	-	-	-
b_{out}	Outer cavity shape exponent	1.9	none	1.5	1.5	1.5	streamline
$z_{in}(AU)$	Inner cavity offset	0	-	-	-	-	-
$z_{out}(AU)$	Outer cavity offset height	100	-	-	-	-	-
$\theta_{open,in}(^\circ)$	Inner cavity opening angle	15	-	-	-	-	-
$\theta_{open,out}(^\circ)$	Outer cavity opening angle	20	-	-	43	16	27
$\theta_{inc}(^\circ)$	Inclination angle	85	60-90	41-81	81	75	89
$\rho_c(g \text{ cm}^{-3})$	Cavity density	0	-	-	1.40×10^{-20}	1.42×10^{-20}	-
$\rho_{amb}(g \text{ cm}^{-3})$	Ambient density	0	-	-	3.838×10^{-22}	1.42×10^{-20}	-

^aAssumes a $0.5M_\odot$ central stellar mass.

